



# Research and development of next generation batteries in the ALCA-SPRING project (JST)

Kei Nishikawa<sup>1</sup> · Akitoshi Hayashi<sup>2</sup> · Kazunori Takada<sup>1</sup> · Yukiko Matsui<sup>3</sup> · Masashi Ishikawa<sup>3</sup> · Masayoshi Watanabe<sup>4</sup> · Shuji Nakanishi<sup>5</sup> · Kohei Shimokawa<sup>6</sup> · Toshihiko Mandai<sup>1</sup> · Tetsu Ichitsubo<sup>6</sup> · Kiyoshi Kanamura<sup>1,7</sup>

Received: 28 February 2025 / Revised: 8 August 2025 / Accepted: 17 October 2025 / Published online: 31 October 2025  
© The Author(s) 2025

## Abstract

The research and development of the next generation batteries promoted by Japan Science and Technology are introduced. The project name is “Advanced Low Carbon Technology Research and Development Program – Specially Promoted Research for Next Generation Batteries (ALCA-SPRING). All-solid-state batteries with oxide or sulfide solid electrolyte, Li air battery, Li sulfur battery, Mg metal battery and Li metal battery were included in this project. Firstly, the concept and target of ALCA-SPRING project is briefly introduced to clarify an importance of next generation batteries. Especially, the most important purpose is the reduction of CO<sub>2</sub> by using next generation batteries. In addition, unique and typical research results are summarized. A lot of new materials have been developed to realize high energy density of batteries. Furthermore, these materials have been applied to cells to confirm their usefulness. For all-solid-state battery with sulfide solid electrolyte, Li sulfur battery, and Li metal battery, the progress in this project accelerated the commercialization for those batteries. On the other hand, for all-solid-state battery with oxide electrolyte, Li air battery and Mg metal battery, the obstacle preventing practical application became clear, and the need for fundamental research to overcome them was confirmed.

**Keywords** All-solid-state batteries · Li-sulfur batteries · Li-air batteries · Mg metal batteries · Li metal batteries

✉ Kei Nishikawa  
NISHIKAWA.Kei@nims.go.jp

<sup>1</sup> Research Center for Energy and Environmental Materials, National Institute for Materials Science, 1-1, Namiki, Tsukuba, Ibaraki 305-0044, Japan

<sup>2</sup> Department of Applied Chemistry, Graduate School of Engineering, Osaka Metropolitan University, 1-1 Gakuen-cho, Naka-ku, Sakai, Osaka 599-8531, Japan

<sup>3</sup> Department of Chemistry and Materials Engineering, Faculty of Chemistry, Materials and Bioengineering, Kansai University, 3-3-35 Yamate-cho, Suita 564-8680, Japan

<sup>4</sup> Institute of Advanced Sciences, Yokohama National University, 79-5 Tokiwadai, Hodogaya-ku, Yokohama 240-8501, Japan

<sup>5</sup> Research Center for Solar Energy Chemistry, Graduate School of Engineering Science, The University of Osaka, 1-3, Machikaneyama, Osaka 560-8531, Japan

<sup>6</sup> Institute for Materials Research, Tohoku University, 2-1-1 Katahira, Aobaku, Sendai 980-8577, Japan

<sup>7</sup> Department of Applied Chemistry for Environment, Tokyo Metropolitan University, 1-1 Minami-Osawa, Hachioji, Tokyo 192-0397, Japan

## 1 Introduction

Rechargeable batteries have been developed to enhance the quality of life. In recent years, they have played a crucial role in various applications, particularly as power sources for electric vehicles and energy storage systems. These applications are essential for reducing carbon dioxide emissions from human activities [1]. Various rechargeable batteries have been used in transportation, consumer electronics, and energy storage. Lead-acid batteries have been widely employed in cars, ships, and energy storage systems. Nickel-cadmium batteries have been utilized in trains and portable electronic devices, while nickel-metal hydride batteries have been used in cell phones and hybrid vehicles. Among rechargeable batteries, lithium-ion batteries (LIBs) have gained significant attention due to their high energy density, especially following their commercialization by Sony. In recent years, LIBs have been increasingly adopted as power sources for electric vehicles (EVs), energy storage systems (ESSs), smartphones, and laptops. In particular,

LIBs for EVs have been extensively developed to enhance battery performance, energy density, and power output. However, the energy density of LIBs for EV applications is approximately  $200 \text{ W h kg}^{-1}$ , which may be insufficient for long-distance driving. Currently, large LIBs have been used in EVs to extend the driving range beyond 500 km per full charge. However, their large volume is undesirable for automobile manufacturers. In the future, achieving higher energy density in batteries will be essential for EVs and other applications. Various rechargeable batteries have been commercialized and utilized across different industries. However, new applications, such as EVs and ESSs, have demanded higher energy density, improved safety, longer life cycles, and enhanced performance, as previously discussed [2]. Among conventional rechargeable batteries, LIBs remain the most promising candidate. For future applications, significantly higher battery performance will be required. Recently, next-generation batteries have gained considerable attention due to their high energy density. Figure 1 presents the energy density of LIBs and other rechargeable batteries, including next-generation alternatives. The energy density of LIBs was estimated based on a full-cell configuration. The dotted curve represents the energy density calculated from the operating voltage and the cathode material's capacity. These estimated energy densities were approximately one-third of the values calculated from the operating voltage and cathode capacity. In the ALCA-SPRING project, energy density was identified as the top

priority, with a final target of  $500 \text{ W h kg}^{-1}$ . Among various next-generation batteries, only lithium-air batteries were expected to achieve  $500 \text{ W h kg}^{-1}$  or higher, while other next-generation batteries were projected to range between 300 and  $450 \text{ W h kg}^{-1}$ . In addition to energy density, safety and cycle life were critical considerations. Based on these requirements, the selected rechargeable batteries for future applications included all-solid-state batteries with oxide or sulfide solid electrolytes, lithium-sulfur batteries, lithium-air batteries, magnesium-metal batteries, and lithium-metal batteries. At the project's initial stage, other rechargeable battery types, such as anion-shuttle batteries and zinc-anode batteries, were also considered. However, research on these batteries was discontinued after the first-stage evaluation. Subsequently, the focus shifted to the five selected battery types. This review summarizes significant research findings on all-solid-state batteries with oxide or sulfide solid electrolytes, lithium-sulfur batteries, lithium-air batteries, magnesium-metal batteries, and lithium-metal batteries. In addition, Table 1 summarizes the characteristics of the five battery types from perspectives of energy density, safety, cycle life, cost, supply chain, resource environment, and mass productivity. Each battery has advantages and disadvantages, then, the research progress is strongly expected.

Research on next-generation batteries has been conducted through various national projects. The European Battery Innovation project, involving 12 participating countries and primarily led by Germany, had a total budget of up to

**Fig. 1** Energy densities of next-generation batteries and lithium-ion batteries

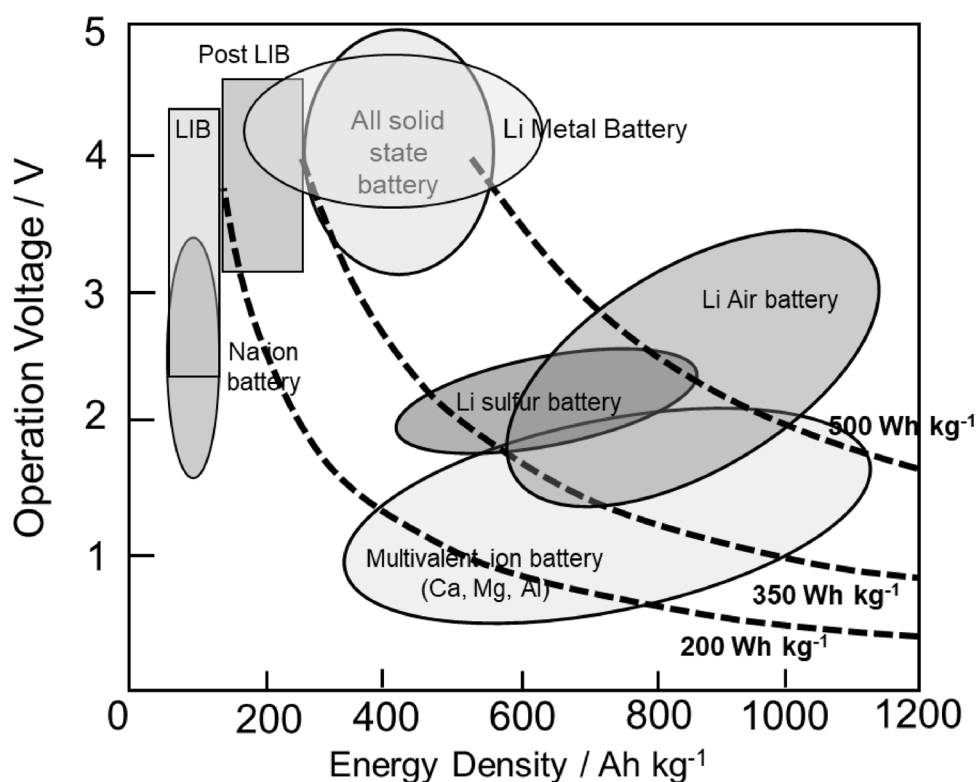


**Table 1** Table evaluating six battery systems on seven criteria. As for the Mg metal battery, the material has not yet been decided, and the evaluation of costs, supply chains, etc. it still uncertain

	<i>Energy Density (Wh/kg)</i>	<i>Safety</i>	<i>Cycle Life</i>	<i>Cost</i>	<i>Supply Chain</i>	<i>Resource Environment (not CO<sub>2</sub> LCA)</i>	<i>Mass Productivity</i>
Solid-State (Sulfide)	○	○ *Concern about S	○ *Concern about volume change	△	○	Li, S, Cl, Mn, Ni, Co	△
Solid-State (Oxide)	○	◎	○ *Concern about volume change	△	△	Li, La, Zr, Mn, Ni, Co	△
Li-S	○	○ *Concern about S	○	◎	○	Li, S, F	○
Li-Air	◎	○	△	◎	○	Li, F	○
Mg	△	◎	△	○ *many undetermined factors	○ *many undetermined factors	Cannot be evaluated *many undetermined factors	△ *many undetermined factors
Li-metal	◎	○	○	○	△ *Same situation as LIBs	Li, Mn, Ni, Co, F	○

2.9 billion euros. This large-scale initiative integrated industry, government, and academia, focusing on strengthening supply chains, recycling, and life cycle assessment (LCA). The primary targets were LIBs and solid-state batteries [3]. In Germany, the Solstice project investigated sodium-zinc molten salt batteries for low-cost stationary storage. This initiative, supported by the Horizon 2020 program with 7.7 million euros, focused on Na-Zn battery development under the leadership of the Helmholtz Association of German Research Centers [4]. In France, the France 2030 project aimed to increase EVs production and received 3.6 billion euros in funding [5]. In the United Kingdom, the Faraday Battery Challenge supported research activities at the Faraday Institution, covering all stages from basic research to commercialization. This project, with a total budget of £610 million until 2025, targeted LIBs, all-solid-state batteries, lithium-sulfur batteries, and multivalent ion batteries [6]. In the United States, the Joint Center for Energy Storage Research was led by Argonne National Laboratory and focused on multivalent ion and lithium-sulfur batteries. The project received \$120 million in funding from the Department of Energy over five years, concluding in 2023. Additionally, the Battery500 Consortium, a research initiative centered at Pacific Northwest National Laboratory, focused on lithium-metal battery development [7].

## 2 Concept of the ALCA-SPRING project

A critical aspect of battery technology is the material science behind anode and cathode materials. To date, many researchers have developed new materials to enhance battery performance, including cycle life, power density, energy density, and safety. One of the most significant advancements was the commercialization of LIBs, which offer higher energy and power densities than conventional batteries. Their high energy density makes them ideal for portable applications such as smartphones and laptop computers. More recently, large-scale LIBs have been deployed in EVs and ESSs. However, EVs require rechargeable batteries with significantly higher energy densities to achieve longer driving ranges. Similarly, ESSs demand more compact and efficient battery solutions. The energy density of LIBs is constrained by the capacity densities of cathode and anode materials. To develop rechargeable batteries with higher energy densities, new electrode materials with greater capacity densities—such as oxygen in air, sulfur, high-nickel oxides, silicon, and lithium—must be explored. These novel cathode and anode materials contribute to improvements in specific gravimetric energy density [8]. In addition, volumetric energy density is crucial for applications in EVs and ESSs. The rechargeable batteries used in these applications are typically large battery packs composed of multiple cells, as illustrated in Fig. 2. When LIBs are used as unit cells, additional space must be allocated within the battery pack for a cooling system. This is because LIBs exhibit poor cycle life at high temperatures (above 60 °C) due to the low stability of liquid electrolytes [9]. In contrast, solid electrolytes in all-solid-state

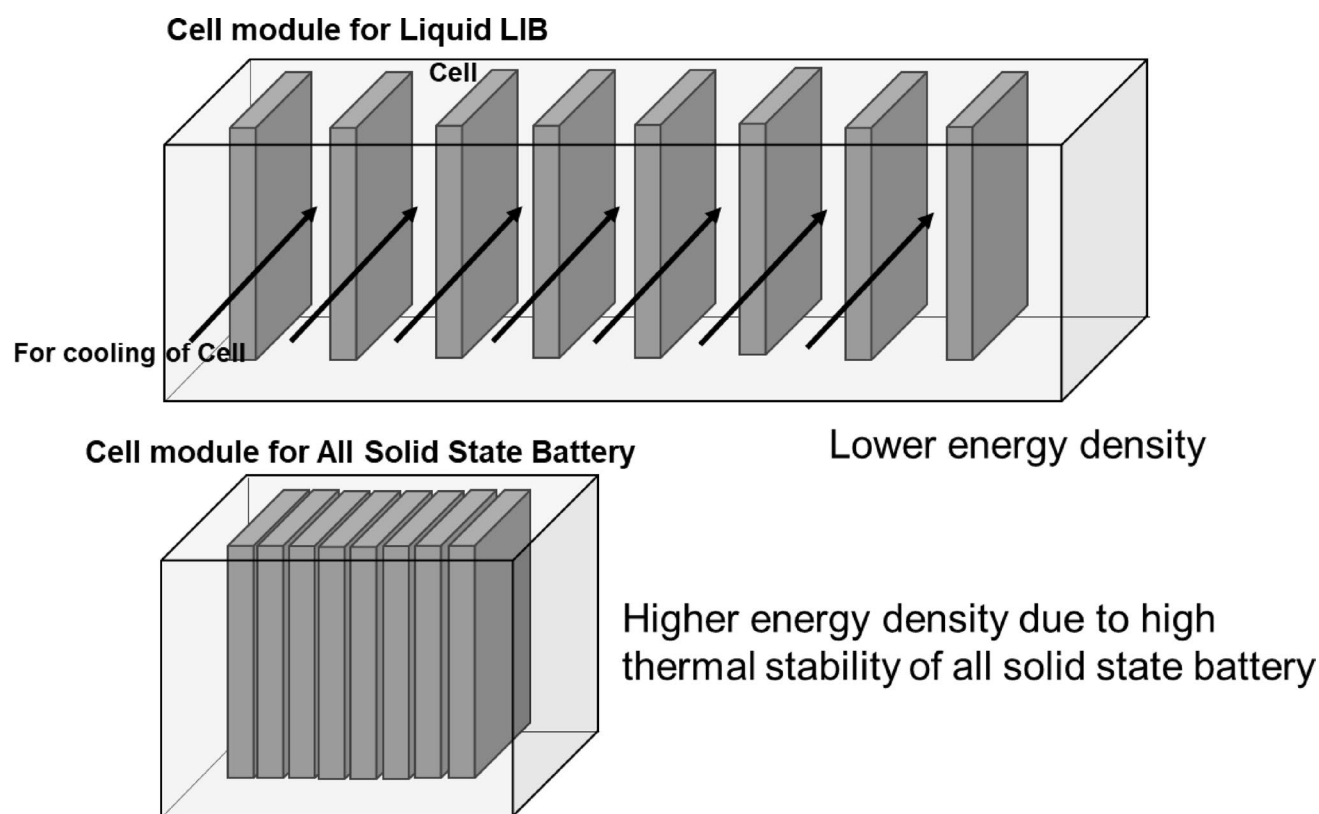


**Fig. 2** Battery pack containing multiple cells with liquid and solid electrolytes for electric vehicles

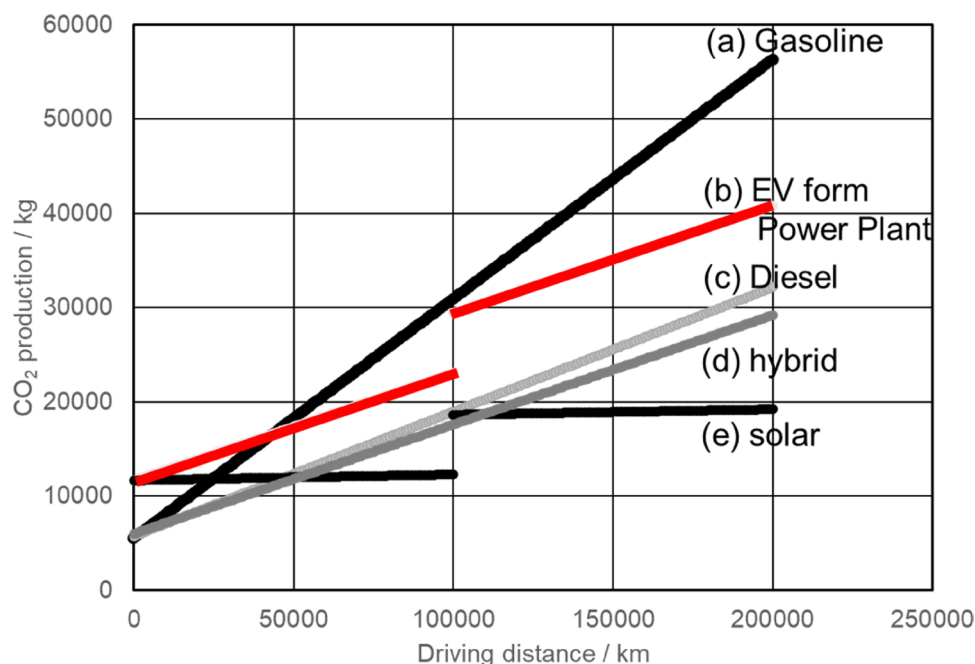
batteries (ASSBs) offer excellent stability at elevated temperatures, such as 100 °C. This enhanced thermal stability reduces the need for cooling system space within the battery pack, thereby increasing volumetric energy density.

To achieve higher gravimetric and volumetric energy densities, new electrode designs and innovative cell preparation concepts must be developed. In this project, the primary research objective was the development of new materials for next-generation batteries based on a cell design concept. Although many materials have been investigated for both next-generation batteries and LIBs, only a few have been successfully implemented in commercial cells. This underscores the need for material evaluation using pouch cells with relatively high capacities, such as 50 mAh. The assessment of a cell's energy and power densities can be conducted more accurately using such pouch cells, as they account for cell configuration factors. In the ALCA-SPRING project, research and development efforts focused on next-generation battery materials, along with evaluations of energy density and other characteristics in prototype cells. This research framework provides a clearer understanding of the critical factors necessary to achieve the target performance of commercial rechargeable batteries.

### 3 Research targets for next-generation batteries based on life cycle assessment (LCA) of CO<sub>2</sub> for rechargeable batteries

The requirements for next-generation batteries were analyzed using the LCA of CO<sub>2</sub> emissions. LCA calculations for vehicles were performed and are presented in Fig. 3. The LCA results varied by country due to differences in electricity generation sources. Additionally, CO<sub>2</sub> emissions from power plants depended on each country's energy mix, which included nuclear, hydroelectric, thermal, renewable, and biomass power plants [10]. In Japan, the CO<sub>2</sub> emission factor was 0.54 kg kWh<sup>-1</sup>. Figure 3 illustrates LCAs for four types of vehicles using different fuel sources. For gasoline- and diesel-powered vehicles, CO<sub>2</sub> emissions at zero driving distance corresponded to the combined emissions from vehicle production and disposal (or recycling) processes. As the driving distance increased, total CO<sub>2</sub> emissions also increased. This corresponds to CO<sub>2</sub> production from fuel combustion. In the cases of EVs and hybrid electric vehicles (HEVs), CO<sub>2</sub> emissions at zero driving mileage correspond to the sum of CO<sub>2</sub> generated from vehicle production, vehicle disposal (or recycling), and battery production processes. For EVs, CO<sub>2</sub> emissions increase with driving mileage due to electricity generation from power

**Fig. 3** Life cycle assessment of CO<sub>2</sub> emissions for various vehicle types: (a) gasoline engine car, (b) pure electric vehicle, (c) diesel engine car, (d) hybrid vehicle, and (e) electric vehicle powered by renewable energy



plants. In contrast, HEV emissions are comparable to those of internal combustion engine vehicles. During the first 4.5 years, CO<sub>2</sub> emissions from gasoline-powered vehicles are lower than those from EVs. This indicates that total CO<sub>2</sub> emissions from gasoline vehicles and EVs become equivalent after nine years. Thus, EVs do not contribute to CO<sub>2</sub> reduction within this period. This undesirable outcome is primarily due to the high CO<sub>2</sub> emissions associated with battery production. The CO<sub>2</sub> emissions from battery production are influenced by the energy density of rechargeable batteries: higher energy density reduces the total material required, thereby lowering CO<sub>2</sub> emissions. Another critical factor is battery replacement in EVs, which significantly impacts overall CO<sub>2</sub> emissions. In Fig. 3, the lifespan of rechargeable batteries is assumed to be 10 years, leading to a noticeable increase in CO<sub>2</sub> emissions at that point. This highlights the need for improving battery longevity. Finally, the introduction of CO<sub>2</sub>-free electricity sources, such as renewable energy, is essential for reducing emissions. Currently, the primary renewable energy sources are solar and wind power. These energy sources strongly depended on weather and seasonal variations. Additionally, solar energy was only available during the daytime. To integrate these renewable energy sources effectively, a rechargeable battery serving as a buffering system (energy storage system, ESS) was essential [11]. The production of rechargeable batteries for ESS also needed to minimize CO<sub>2</sub> emissions.

In summary, the LCA of vehicles identified three major challenges for next-generation battery research:

(i) Higher energy density.

(ii) Longer cycle life.

(iii) Suitability for ESS.

Currently, LIBs have been used in both EVs and ESS. However, the performance of next-generation batteries must surpass that of LIBs to address these challenges.

Another critical consideration was material security. Lithium (Li) resources were limited, yet most next-generation batteries still relied on Li. Therefore, alternative materials such as magnesium (Mg), sodium (Na), and potassium (K) were explored to address resource limitations. In this project, Mg metal batteries were investigated as a potential next-generation battery. Due to the divalent nature of Mg ions, Mg metal batteries theoretically offered twice the capacity of LIBs.

#### 4 All-solid-state battery with sulfide solid electrolyte

All-solid-state batteries (ASSBs) with solid electrolytes have attracted global attention due to their enhanced safety high rate capability, high energy density and long cycle life [12–14]. In particular, sulfide solid electrolytes offer a range of advantages, including excellent electrical and mechanical properties, making them well-suited for all-solid-state batteries. The crystalline LGPS-type  $\text{Li}_{9.54}[\text{Si}_{0.6}\text{Ge}_{0.4}]_{1.7}\text{P}_{1.44}\text{S}_{11.1}\text{Br}_{0.3}\text{O}_{0.6}$  shows a superior lithium-ion conductivity of  $3.2 \times 10^{-2} \text{ S cm}^{-1}$  at 25 °C [15]. The  $\text{Li}_2\text{S-P}_2\text{S}_5$  glasses have relatively high conductivity, ranging from  $10^{-4}$  to  $10^{-3} \text{ S cm}^{-1}$ , along with excellent formability. Sulfide



glassy powders can be readily compacted and densified through cold-pressing, eliminating the need for heat treatment and promoting close, extensive interfacial contact between the electrode and electrolyte [16].

All-solid-state Li/S batteries with the combination of a sulfur positive electrode and a Li metal negative electrode have gained significant interest for their high energy density. Sulfur and its discharge compound,  $\text{Li}_2\text{S}$ , are promising cathode active materials; however, their insulating nature necessitates the addition of solid electrolytes and conductive carbon additives to the cathode layer to establish ionic and electronic conducting pathways. In contrast, electrode–electrolyte bifunctional materials in the  $\text{Li}_2\text{S} - \text{V}_2\text{S}_3 - \text{LiI}$  system exhibit high ionic and electronic conductivities. As a result, ASSBs utilizing these bifunctional materials in the cathode layer operated without requiring additional solid electrolytes or conductive carbon additives. As shown in Fig. 4(a) and (b), an all-solid-state battery incorporating a mechanochemically prepared  $90(0.75\text{Li}_2\text{S} \cdot 0.25\text{V}_2\text{S}_3) \cdot 10\text{LiI}$  (mol%) cathode demonstrated a high capacity of  $370 \text{ mAh g}^{-1}$  at  $25^\circ\text{C}$ , with 83% capacity retention after 100 cycles [17]. The concept of electrode–electrolyte bifunctional materials presents significant potential for increasing the energy density of ASSBs.

The application of Li metal anodes was essential for achieving all-solid-state Li/S batteries; however, short-circuiting due to Li dendrite formation remained a significant challenge. To maintain the electrode–electrolyte interface with electrode volume changes during charge–discharge cycling, and chemo-mechanical properties of solid electrolytes are important [18]. The chemical degradation of the sulfide electrolytes due to reduction is a trigger of short-circuiting. The incorporation of LiI into  $\text{Li}_3\text{PS}_4$  enhances

reduction tolerance and effectively mitigates side reactions with lithium metal. The  $54\text{Li}_3\text{PS}_4 \cdot 46\text{LiI}$  (mol%, LPSI) glass exhibits higher conductivity of  $10^{-3} \text{ S cm}^{-1}$ , lower Young's modulus and better reduction tolerance to Li metal than the  $\text{Li}_2\text{S} - \text{P}_2\text{S}_5$  glasses [19]. A Li symmetrical cell utilizing the LPSI glass electrolyte was reversibly cycled without short-circuiting at a current density of  $1.25 \text{ mA cm}^{-2}$  for 3,400 h at  $100^\circ\text{C}$  [20]. To suppress void formation at the Li metal interface during the Li stripping/plating process, the optimal stack pressure was determined to be 3–10 MPa, ensuring cycle stability [21]. In addition, the incorporation of a Sn interlayer at the interface between Li metal and the  $\text{Li}_3\text{PS}_4$  electrolyte improved the Li stripping/plating performance of all-solid-state Li symmetrical cells [22]. Further enhancement in cycling performance was achieved by replacing pure Li metal with a Li-Mg alloy ( $\text{Li}_{0.97}\text{Mg}_{0.03}$ ).

An all-solid-state Li/S cell was fabricated using a  $\text{Li}_{0.97}\text{Mg}_{0.03}$  anode, LPSI glass electrolyte, and a sulfur composite cathode (S–C–LPSI) with a weight ratio of 40:20:40. Figure 5 presents the discharge–charge curves of the  $\text{Li}_{0.97}\text{Mg}_{0.03}/\text{LPSI}/\text{S}-\text{C}-\text{LPSI}$  cell, obtained at a stack pressure of 5 MPa [21]. The operating temperature and current density were  $60^\circ\text{C}$  and  $2.0 \text{ mA cm}^{-2}$  ( $1.33 \text{ C}$ ), respectively. The cell exhibited a maximum capacity of  $1,627 \text{ mAh g}^{-1}$ , approaching the theoretical capacity of sulfur ( $1,672 \text{ mAh g}^{-1}$ ). Additionally, it demonstrated high cycling stability, retaining 95.8% of its initial capacity after 50 cycles.

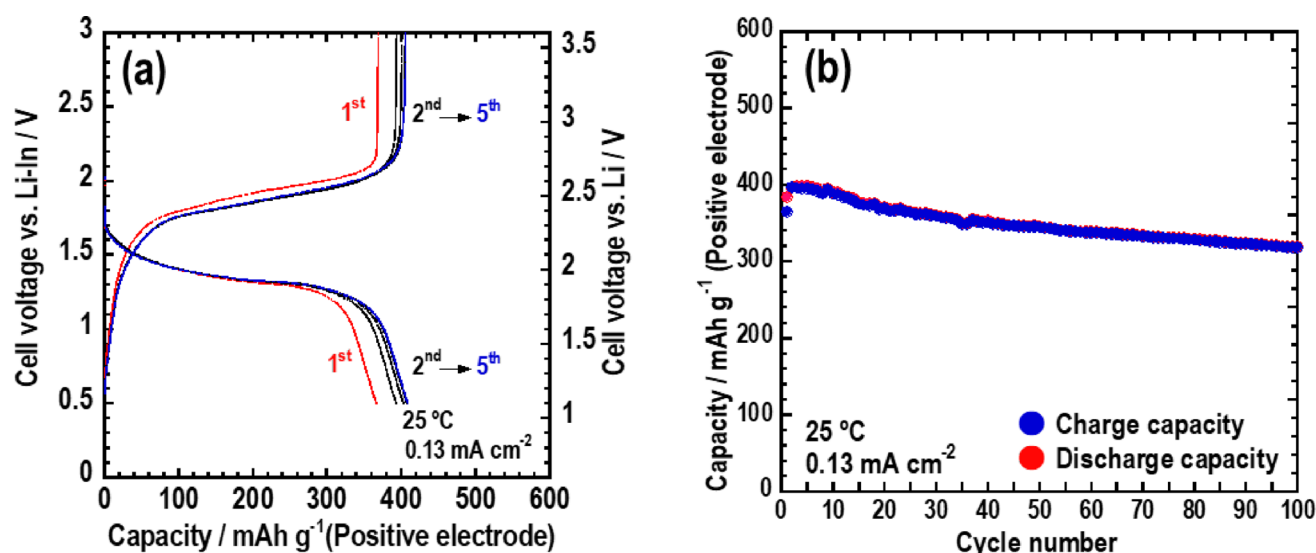


**Fig. 4** (a) Charge–discharge curves over five cycles and (b) cycle performance of the all-solid-state  $\text{Li-In}/\text{Li}_3\text{PS}_4/90(0.75\text{Li}_2\text{S} \cdot 0.25\text{V}_2\text{S}_3) \cdot 10\text{LiI}$  cell. Reproduced from Ref. 17. Copyright 2019 American Chemical Society

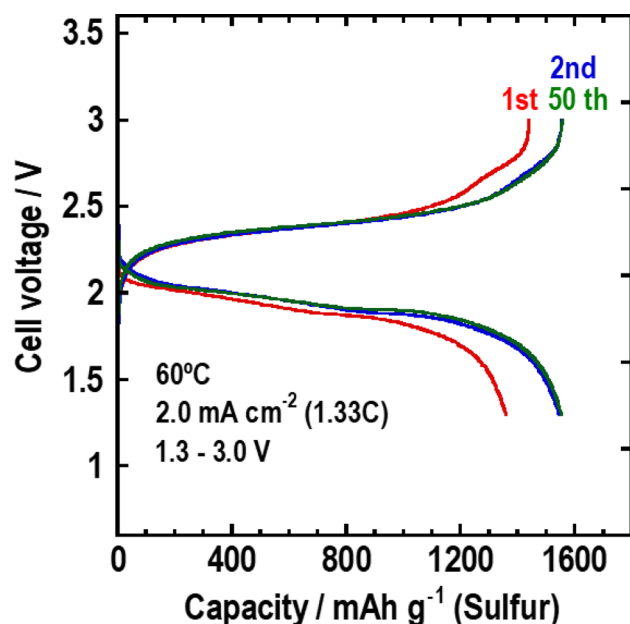


**Fig. 5** Discharge-charge curves of the all-solid-state  $\text{Li}_{0.97}\text{Mg}_{0.03}/54\text{Li}_3\text{PS}_4\cdot 46\text{LiI}/\text{S}$  cell, obtained at a stack pressure of 5 MPa and a temperature of 60 °C. Reproduced from Ref. 21. Copyright 2023 American Chemical Society

## 5 All-solid-state battery with oxide solid electrolyte

Sulfide-based solid electrolytes are typically plastically deformable, allowing their connection with active materials in sulfide-based solid-state batteries through cold pressing. In contrast, oxide-based solid electrolytes are generally rigid, requiring co-sintering to establish contact with active materials. However, high-temperature sintering promotes elemental diffusion between the electrolyte and active materials, leading to the formation of impurity phases at the interface. To address this issue, research on solid-state batteries with oxide-based solid electrolytes in the ALCA-SPRING project aimed to develop oxide electrolytes that could be sintered at lower temperatures to minimize elemental diffusion during co-sintering. Three types of such solid electrolytes were developed, and the charge-discharge properties of the resulting batteries are presented in Fig. 6.

The solid-state battery shown in Fig. 6(a) utilized garnet fine powder as the solid electrolyte [23]. While reducing particle size effectively lowered the sintering temperature, garnet-type solid electrolytes readily reacted with dispersion media used in grinding. To prevent this, the garnet fine powder used in this battery was prepared from a precursor without grinding. Fine powder of  $\text{La}_{2.4}\text{Zr}_{1.2}\text{Ta}_{0.4}\text{O}_7$ , consisting of framework cations, was synthesized using a polymerized complex method. The fluorite-type precursor then reacted with  $\text{Li}_2\text{O}$ , forming a garnet-type solid electrolyte,  $\text{Li}_{6.5}\text{La}_3\text{Zr}_{1.5}\text{Ta}_{0.5}\text{O}_{12}$ , at low temperatures (400–600 °C),

effectively suppressing particle growth [24]. The solid-state battery incorporated  $\text{LiNi}_{1/3}\text{Co}_{1/3}\text{Mn}_{1/3}\text{O}_2$  as the cathode and graphite as the anode. Assembly was performed by hot pressing at 550 °C under 375 MPa.

The solid-state battery shown in Fig. 6(b) utilized a garnet-type solid electrolyte,  $\text{Li}_6\text{La}_3\text{ZrTa}_{0.8}\text{Bi}_{0.2}\text{O}_{12}$ , in which Bi partially substituted Ta [25]. The introduced Bi formed a  $\text{Li}_2\text{O}-\text{Bi}_2\text{O}_3$  molten phase with a low eutectic point of 690 °C upon heating, promoting sintering and reducing the sintering temperature of the garnet-type solid electrolyte to 825 °C. The cathode material was Zn-doped  $\text{LiCoO}_2$ , and the cathode layer was stacked onto the solid electrolyte layer through co-sintering at 850 °C. A Li metal anode was attached to the opposite side of the electrolyte layer with a PEO-based polymer electrolyte interlayer to prevent potential reduction of the solid electrolyte in contact with Li metal.

The solid electrolyte used in the solid-state battery shown in Fig. 6(c) was  $\text{Li}_{3.5}\text{Ge}_{0.5}\text{V}_{0.5}\text{O}_4$ , which has a  $\gamma\text{-Li}_3\text{PO}_4$ -type structure and an ionic conductivity approaching  $10^{-4} \text{ S cm}^{-1}$  [26]. This solid electrolyte remained stable against typical layered cathode materials, such as  $\text{LiCoO}_2$ , even at high temperatures of 700 °C. The solid-state battery was assembled using spark-plasma sintering at 450 °C under 400 MPa. The cathode and anode materials were  $\text{LiNi}_{1/3}\text{Co}_{1/3}\text{Mn}_{1/3}\text{O}_2$  and Li metal, respectively. A PEO-based polymer electrolyte was interposed at the anode interface, as  $\text{Li}_{3.5}\text{Ge}_{0.5}\text{V}_{0.5}\text{O}_4$  was unstable against Li metal. The SEM image of the  $\text{LiNi}_{1/3}\text{Co}_{1/3}\text{Mn}_{1/3}\text{O}_2$  particle (inset) showed that primary particles aggregated into secondary particles with random orientations. This structure helped average the anisotropic volume change during charge and discharge, thereby improving cycle performance. The solid-state battery shown in Fig. 6(a) was cycled at 0.01 C for the cathode at 25 °C, while those in Figs. 6(b) and (c) operated at an elevated temperature of 60 °C due to the use of PEO electrolytes. However, by optimizing electrolyte compositions, their operating temperature has since been reduced to room temperature [27].

Studies on oxide-based solid-state batteries in ALCA-SPRING have been mainly focused on lowering the sintering temperature of battery materials to suppress the reaction between the cathode and electrolyte materials, as mentioned above. Another challenge in the development of oxide-based solid-state batteries is on the anode side, which is realizing Li metal anodes. Lithium metal has a high theoretical capacity and low electrode potential, which provide a high energy density to the batteries as anodes. However, lithium metal tends to grow dendritically during charging, which is a problem in realizing lithium metal anodes, because the dendritic growth results in the internal short-circuit and sometimes leads to thermal runaway. Solid electrolytes are

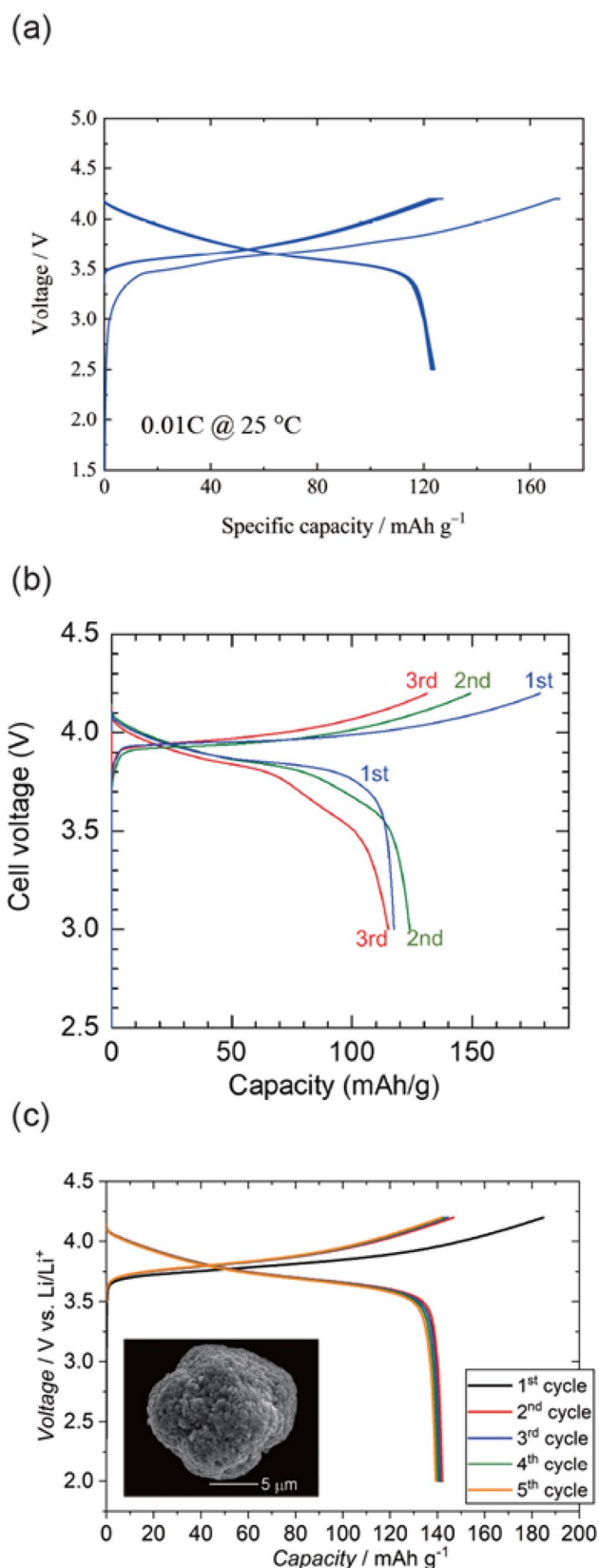


**Fig. 6** Charge-discharge curves of solid-state batteries with oxide solid electrolytes developed in the ALCA-SPRING project. The solid-state batteries in (a), (b), and (c) employed Li<sub>6.5</sub>La<sub>3</sub>Zr<sub>1.5</sub>Ta<sub>0.5</sub>O<sub>12</sub> fine powder, Li<sub>6</sub>La<sub>3</sub>Zr<sub>0.8</sub>Bi<sub>0.2</sub>O<sub>12</sub>, and Li<sub>3.5</sub>Ge<sub>0.5</sub>V<sub>0.5</sub>O<sub>4</sub>, respectively, as solid electrolytes with low sintering temperatures. The cathode and anode material combinations used in these batteries were LiNi<sub>1/3</sub>Co<sub>1/3</sub>Mn<sub>1/3</sub>O<sub>2</sub> | graphite, Zn-doped LiCoO<sub>2</sub> | Li metal, and LiNi<sub>1/3</sub>Co<sub>1/3</sub>Mn<sub>1/3</sub>O<sub>2</sub> | Li metal, respectively. (Reprinted from Ref. 23 Copyright Wiley, from Ref. 25 Copyright Authors, from Ref. 26 Copyright American Chemical Society)

expected to enable us to use lithium metal anodes by acting as solid membranes that block the dendritic growth; however, dendrites grow even through the solid electrolyte layer in solid-state batteries with garnet-type solid electrolytes [28]. While various methods, e.g. surface polishing [29] and heat treatment [30], have been reported for this problem, we have developed a very simple and effective way to suppress the dendritic growth, which is immersion in an aqueous solution of LiOH [31]. As demonstrated in Fig. 7, dendritic growth does not lead to internal short-circuit up to a high current density of 5.0 mA cm<sup>-2</sup> in a Li/garnet/Li symmetric cell with a garnet sintered pellet after the immersion.

In ALCA-SPRING project, we had been developing solid-state batteries employing garnet-type solid electrolytes, because the garnet-type is the only candidate. Ionic conductivities of the order of 10<sup>-3</sup> S cm<sup>-1</sup> among oxides have been achieved only in NASICON [32], perovskite [33], and garnet-type structures [34] before the project was launched. However, the former two are incompatible with lithium metal anodes, because their conductivities reach the order of 10<sup>-3</sup> S cm<sup>-1</sup> only when they contain Ti. On the other hand, new kinds of electrolytes with such high conductivities have emerged, recently: one is LiTa<sub>2</sub>PO<sub>8</sub> [35] and the other is Li<sub>2-x</sub>La<sub>(1+x)/3</sub>M<sub>2</sub>O<sub>6</sub>F (M = Nb, Ta) [36]; especially, bulk conductivity of the latter approaches 10<sup>-2</sup> mS cm<sup>-1</sup>. These solid electrolytes are considered to open up new possibilities of oxide-based solid-state batteries.

## 6 Lithium metal sulfur battery (Li-S)

Lithium-sulfur (Li-S) batteries are promising next-generation secondary batteries due to sulfur's high energy capacity and abundance [37–39]. However, the dissolution of lithium polysulfides (Li<sub>2</sub>S<sub>x</sub>) into the electrolyte has hindered their performance. In the ALCA-Spring study, we addressed this issue by developing a Li<sub>2</sub>S<sub>x</sub>-insoluble cell. Specifically, we (1) designed an electrolyte that prevented Li<sub>2</sub>S<sub>x</sub> dissolution [40–43] while enhancing the reversibility of the lithium anode [44–47], and (2) developed a cathode that encapsulated sulfur within microporous carbon to mitigate dissolution. As a result, we achieved a gravimetric energy density of 350 Wh kg<sup>-1</sup>.



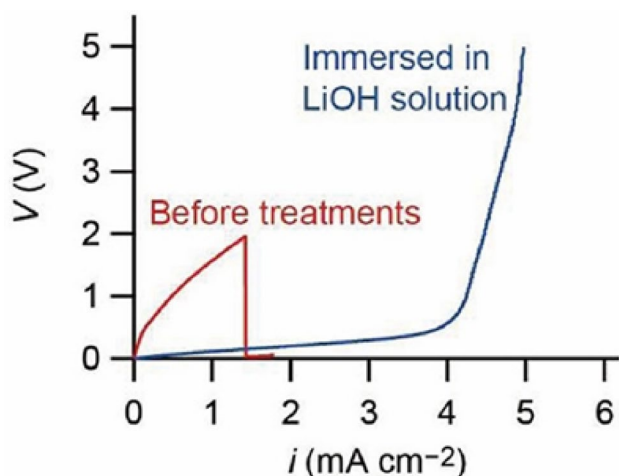


**Fig. 7** *i*-*V* characteristics of Li/garnet sintered pellet/Li symmetric cells obtained by chronopotentiometry with a ramp-up current rate of  $1 \text{ mA cm}^{-2} \text{ min}^{-1}$ . The cell assembled with the as-purchased garnet pellet shows an abrupt voltage drop indicating the internal short-circuit at the current density of  $1.4 \text{ mA cm}^{-2}$ , while the cell with the pellet after immersion in an aqueous solution of LiOH does not reach the internal short circuit up to  $5.0 \text{ mA cm}^{-2}$ . (Reprinted from Ref. 31 Copyright Authors.)

Among lithium polysulfides,  $\text{Li}_2\text{S}_x$  ( $x = 8-2$ ),  $\text{Li}_2\text{S}_8$  is the most soluble species [41]. Our investigations revealed that its solubility was significantly influenced by the donor number (DN) of the electrolyte (Fig. 8(a)) [48]. When the DN was 15 or lower,  $\text{Li}_2\text{S}_8$  solubility dropped below 100 mM. In aprotic ionic liquids (ILs), the DN was governed by the anion; anions with high Lewis basicity, such as  $[\text{CF}_3\text{SO}_3]^-$  or  $[\text{N}(\text{CN})_2]^-$ , led to significantly higher  $\text{Li}_2\text{S}_8$  solubility [49]. A similar trend was observed in solvate ionic liquids,  $[\text{Li}(\text{Glyme})]\text{X}$  [50]. Furthermore, in  $[\text{Li}(\text{G4})_m][\text{TFSA}]$  (G4: tetraglyme), when  $m > 1$ ,  $\text{Li}_2\text{S}_8$  solubility increased markedly [41]. This suggested that at high salt concentrations—where the coordination site-to- $\text{Li}^+$  ratio was lower than the coordination number of  $\text{Li}^+$  (4–5)—the DN of the electrolyte decreased and became dominated by the anion's DN.

We investigated the performance of Li–S coin cells using solvate ILs ( $[\text{Li}(\text{G4})][\text{TFSA}]$ ) and sulfolane-based concentrated electrolytes ( $[\text{Li}(\text{SL})_2][\text{TFSA}]$ ), both of which exhibited extremely low  $\text{Li}_2\text{S}_x$  solubility (Fig. 8(b)) [42]. Due to this low solubility, both systems achieved Coulombic efficiencies exceeding 98%, effectively suppressing the shuttle effect caused by dissolved  $\text{Li}_2\text{S}_x$ . Interestingly, despite its lower ionic conductivity and higher viscosity compared to  $[\text{Li}(\text{G4})][\text{TFSA}]$ ,  $[\text{Li}(\text{SL})_2][\text{TFSA}]$  demonstrated superior rate performance [42]. A notable finding was that in SL-based electrolytes, the  $\text{Li}^+$  diffusion coefficient was the highest among the solution's chemical species ( $\text{Li}^+$ ,  $[\text{TFSA}]^-$ , SL) [42, 51]. This suggested that  $\text{Li}^+$  ions moved by hopping between coordination sites, exchanging ligands with  $\text{TFSA}^-$  and SL. This behavior was likely due to a solution

structure in which SL and  $[\text{TFSA}]^-$  coordinated  $\text{Li}^+$  in a bridging manner [42, 52].

To achieve a high gravimetric energy density ( $> 300 \text{ Wh kg}^{-1}$ ), maintaining a sulfur loading of  $\geq 4 \text{ mg cm}^{-2}$  and an electrolyte-to-sulfur (E/S) ratio of  $\leq 5 \text{ } \mu\text{L mg}^{-1}$  was essential [53]. We found that adding titanium black effectively addressed this requirement [54]. Furthermore, by diluting the G4- and SL-based concentrated electrolytes with non-coordinating solvents such as hydrofluoroether (HFE), we developed localized concentrated electrolytes [41, 43]. These electrolytes preserved the advantages of the concentrated systems while improving ionic conductivity and reducing viscosity. Using a high sulfur-loading electrode ( $4.2 \text{ mg cm}^{-2}$ ) and an SL-based localized concentrated electrolyte, we fabricated a pouch cell under an ultra-low E/S ratio of  $3.0 \text{ } \mu\text{L mg}^{-1}$ . This cell achieved a high energy density of  $350 \text{ Wh kg}^{-1}$  (Fig. 8(c)) [53].

To mitigate structural changes in the sulfur composite cathode, we replaced conventional spherical hollow carbon (Ketjen Black, KB) with mesoporous carbon nanodendrite (MCND), which has a dendritic structure and superior electronic conductivity. Figures 8(d) and (e) show the charge-discharge profiles and cycling performance of a  $> 3 \text{ Ah}$  pouch cell with a high sulfur-loading electrode ( $5.5 \text{ mg cm}^{-2}$ ) utilizing MCND. This was paired with the electrolyte  $[\text{Li}(\text{SL})_2][\text{TFSA}_{0.9}\text{FSA}_{0.1}] + 2\text{HFE}$  at a low E/S ratio of  $3.5 \text{ } \mu\text{L mg}^{-1}$  [55, 56].

We adopted a strategy of combining sulfur with microporous activated carbon (pore diameter  $\leq 2 \text{ nm}$ ) to stabilize sulfur and its reaction intermediates. Figure 9(a) shows the pore distribution of the first-generation microporous activated carbon, which had a specific surface area of approximately  $780 \text{ m}^2 \text{ g}^{-1}$  and a pore diameter between 0.7 and 2.0 nm [57]. Figure 9(b) illustrates the composite of microporous activated carbon and sulfur, where the activated carbon contained 29% sulfur [57]. We investigated the rate characteristics using various electrolytes (Fig. 9(c)), including  $\text{LiPF}_6/\text{EC}$ : DMC,  $\text{LiTFSI}/\text{G4}/\text{HFE}$ ,  $\text{LiFSI}/\text{G4}/\text{HFE}$ , and  $\text{LiFSI}/\text{G4}$  (with molar ratios indicated in the figure). The results demonstrated that reversible sulfur cycling with high-rate characteristics was achievable regardless of the electrolyte type when sulfur was combined with microporous carbon [57].

To increase sulfur content, we utilized alkali-activated azulmic carbon (AZC), a high-surface-area carbon with micropores and some mesopores [58]. When combined with sulfur, AZC enabled a sulfur loading of over 50 wt% [58]. The electrolyte used was a fluorine-substituted system ( $\text{LiTFSI}/\text{FEC}$ : HFE), which underwent reduction on the sulfur cathode during the first discharge, forming a protective film [59]. Figure 9(d) presents the performance of the AZC (S-55%) cathode using two electrolytes: 1 M  $\text{LiTFSI}/\text{FEC}$ :

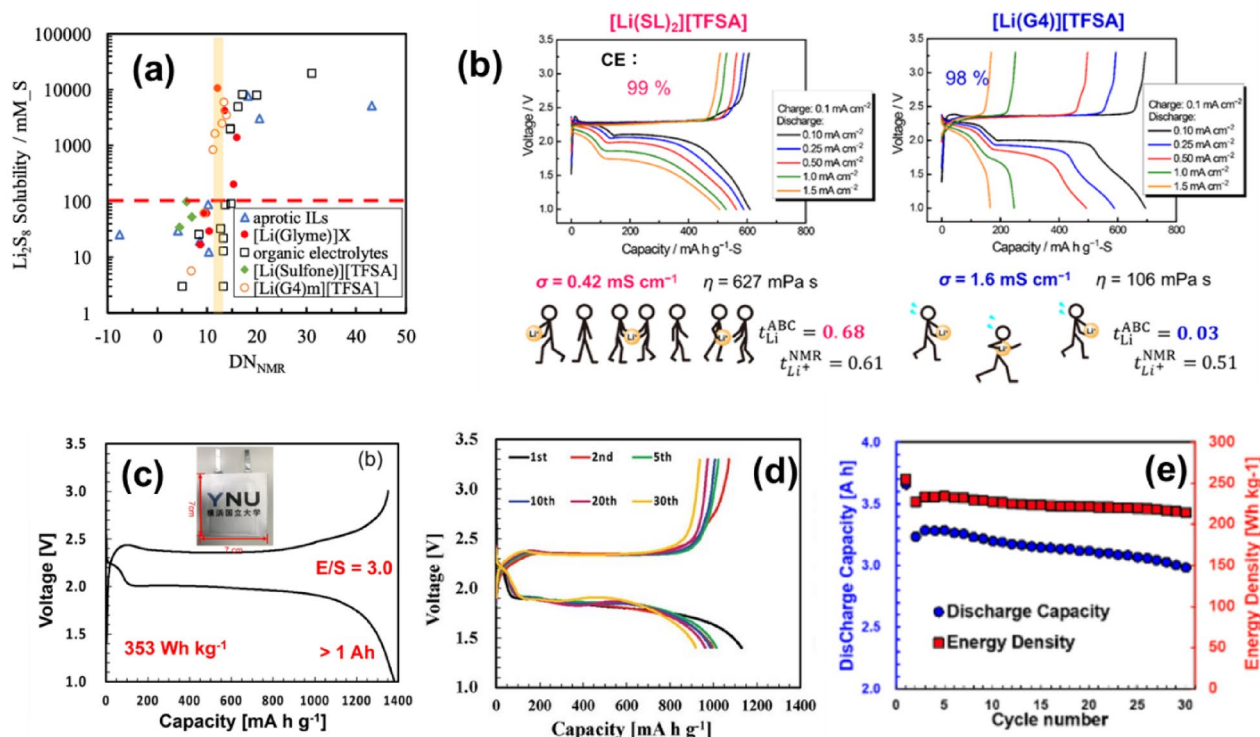


**Fig. 8** (a) Relationship between the solubility of  $\text{Li}_2\text{S}_8$  and the donor number estimated from  $^{23}\text{Na}$ -NMR ( $\text{DN}_{\text{NMR}}$ ) for aprotic IL, organic electrolytes, [Li(glyme)]X, [Li(G4)m][TFSA], and [Li(sulfone)][TFSA]. The horizontal dotted line represents the solubility limit of  $10^2 \text{ mM}_\text{S}$ . Redrawn from Ref. 73. (b) Discharge and charge curves, along with the average Coulombic efficiency at different discharge current densities, for Li|S coin cells with [Li(SL)<sub>2</sub>][TFSA] and [Li(G4)][TFSA] electrolytes. The transport properties of these electrolytes are also presented. Reproduced from Ref. 42. Copyright 2019 American Chemical Society. (c) Initial discharge ( $137 \mu\text{A cm}^{-2}$ , 0.02 C) and

charge ( $343 \mu\text{A cm}^{-2}$ , 0.05 C) curves of a laminated Li-S pouch cell, demonstrating an energy density of  $> 350 \text{ Wh kg}^{-1}$  under high S-loading ( $4.2 \text{ mg cm}^{-2}$ ) and lean electrolyte ( $\text{E/S} = 3.0 \text{ mL mg}_\text{S}^{-1}$ ) conditions. Reprinted from Ref. 53. Copyright 2022 Wiley. (d) Discharge and charge profiles at a charge/discharge current density of  $460 \mu\text{A cm}^{-2}$  for a large-format Li-S pouch-type cell ( $> 3 \text{ Ah}$ , S-loading:  $5.5 \text{ mg cm}^{-2}$ ,  $\text{E/S} = 3.5 \text{ mL mg}_\text{S}^{-1}$ ). Reprinted from Ref. 56. Copyright 2023 Wiley. (e) Discharge capacity and energy density as a function of cycle number for the cell shown in (d). Reprinted from Ref. 53. Copyright 2023 Wiley

HFE (50:50 v/v) + VC (10 vol%) and 2 M  $\text{LiPF}_6/\text{EC} : \text{DMC}$  (30:70 v/v) + VC (10 vol%) [60]. This system achieved a discharge capacity of  $505 \text{ mAh g}^{-1}$  after 300 cycles.

To enhance sulfur capacity utilization, we modified the surface physical properties of porous carbon. Figures 9(e) and 9(f) show the effect of increasing the reaction area by grinding second-generation microporous activated carbon (AC), which supported 48–60 wt% sulfur, using a dry ball mill. This treatment improved the discharge capacity [60]. Additionally, after ball milling, AC was oxidized in 6 M  $\text{HNO}_3$ , increasing the surface oxygen content from 11.7 to 15.7 at%. This modification significantly enhanced the discharge capacity of sulfur [60, 61]. Finally, a sulfur cathode was fabricated using third-generation microporous AC (48–60 wt% sulfur capacity), and the developed amide/DME-based electrolyte ( $\text{LiFSI/DME/HFE}$ ) was applied (Fig. 9(g)). This system maintained high discharge capacity over 400 cycles at a high rate of 0.5 C [62, 63].

Global efforts toward the development of Li-S batteries have intensified, with several leading institutions and

companies advancing unique approaches. In South Korea, research institutions such as the Korea Institute of Science and Technology (KIST) are exploring advanced materials to enhance cycle stability and suppress the polysulfide shuttle effect [64]. German innovation is led by the Fraunhofer Institute, which focuses on scalable manufacturing techniques and the integration of conductive additives to improve the sulfur cathode's conductivity and life span [65]. In the United Kingdom, the Faraday Institution heads the LiSTAR project, targeting critical issues like low Coulombic efficiency and cathode degradation through the design of novel electrolytes and protective interlayers [66]. Australia's Monash University has attracted attention by developing Li-S batteries with ultra-high capacity and long cycle life, achieved through a unique binder and carbon host framework that enables efficient sulfur utilization [67]. In the United States, Lyten Inc. is pioneering 3D graphene-based Li-S batteries aimed at electric vehicles and aerospace sectors, offering high energy density, lightweight structure, and improved safety compared to traditional lithium-ion

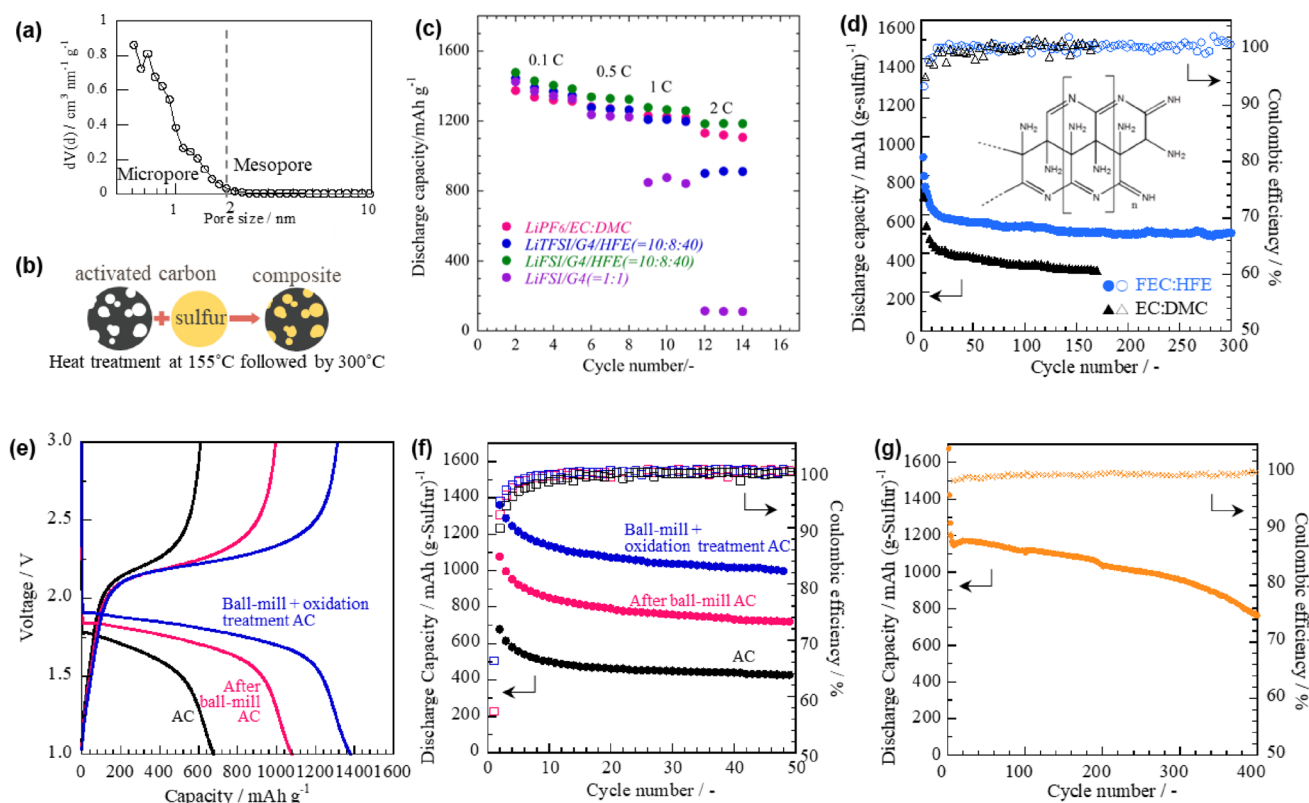


**Fig. 9** (a) Pore-size distribution of a microporous activated carbon by the DFT method. (b) Schematic of the microporous activated carbon–S composite cathode preparation. (c) C-rate performance of the microporous activated carbon–S composite cathode with  $\text{LiPF}_6/\text{EC:DMC}$ ,  $\text{LiTFSI/G4/HFE}$ ,  $\text{LiFSI/G4/HFE}$ , and  $\text{LiFSI/G4}$  electrolytes. (d) Structure of azulmic acid (AZA) and cycle performance of laminate cell containing Li anode and the activated azulmic carbon (AZC)–S

composite cathode with  $\text{LiTFSI/FEC:HFE}$  and  $\text{LiPF}_6/\text{EC:DMC}$  electrolytes. (e) 2nd discharge–charge curves and (f) cycle performance of gen-2 microporous activated carbon (AC)–S, ball-milled AC–S, and ball-milled and oxidized AC–S cathodes in  $\text{LiTFSI/G4/HFE}$ . (g) Cycle performance of gen-3 microporous activated carbon–S cathode with  $2.4\text{ mol dm}^{-3}\text{ LiFSI} + 0.1\text{ mol dm}^{-3}\text{ LiDFOB/DME/HFE}$  electrolyte at 0.5/0.5 C-rate

systems [68]. Each of these global efforts reflects distinct research priorities—ranging from materials innovation and electrolyte design to practical manufacturability and commercial deployment. Together, they illustrate the collaborative international push to unlock the full potential of Li–S batteries as a sustainable, high-energy alternative to current lithium-ion technologies.

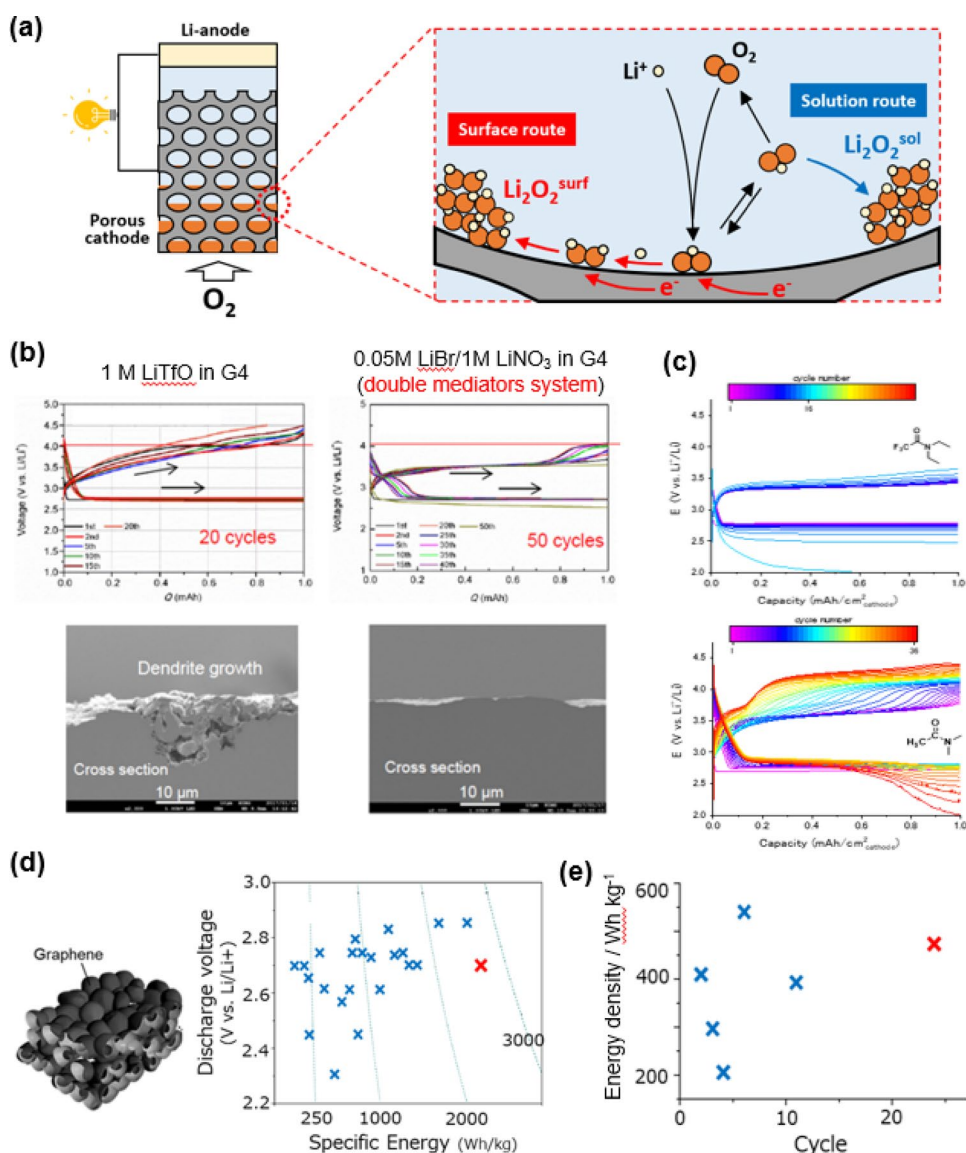
Despite their high theoretical energy density, lithium-sulfur (Li–S) batteries face key commercialization barriers, including the polysulfide shuttle effect, poor cycle life, and low Coulombic efficiency. There is a trade-off between achieving high sulfur loading and maintaining structural stability and conductivity of the cathode. Additionally, the insulating nature of sulfur and its discharge products limits rate performance. Overcoming these challenges requires innovations in cathode architecture, electrolyte design, and interfacial engineering [69].

## 7 Lithium metal air battery (Li–Air)

Lithium–air batteries (Li– $\text{O}_2$  batteries) have emerged as a promising candidate for next-generation rechargeable batteries, owing to their potential to exceed the gravimetric energy density of conventional lithium-ion batteries. Moreover, the use of transition-metal-free cathode materials and the absence of high-temperature sintering steps in electrode fabrication are expected to significantly reduce greenhouse gas (GHG) emissions during production. Typical lithium–air batteries consist of a porous carbon cathode, a lithium metal anode, and an electrolyte-separated by a separator. During discharge, oxygen reduction generates lithium peroxide ( $\text{Li}_2\text{O}_2$ ) within the porous cathode, which undergoes reversible oxidation during charging (Fig. 10(a)). Although significant progress has been made in elucidating the detailed reaction mechanisms and side reactions involved in the charge–discharge processes [70–73], achieving sufficient cycling performance under the benchmark condition of  $500\text{ Wh kg}^{-1}$  remains a major challenge. Our project aimed to enhance cycle performance while achieving a



**Fig. 10** (a) Schematic illustration explaining the discharge reactions of a lithium-air (lithium-oxygen) battery. (b) Discharge-charge cycle profile and cross-sectional SEM image of the lithium anode obtained using an electrolyte containing dual-anion redox mediators ( $\text{LiNO}_3 + \text{LiBr}$ /tetraglyme) (right). The cycle profile under the same conditions in a  $\text{LiBr}/\text{LiCF}_3\text{SO}_3$  electrolyte is shown for comparison (left). Reprinted with permission from Ref. 74. Copyright 2017 American Chemical Society. (c) Discharge-charge cycle profile obtained in a  $\text{LiNO}_3$ /dimethylacetamide electrolyte (top). The cycle profile under the same conditions in a  $\text{LiNO}_3$ /tetraglyme electrolyte is shown for comparison (bottom). Reprinted with permission from Ref. 76. Copyright 2024 American Chemical Society. (d) Discharge voltage plotted against specific energy. The red cross and blue crosses indicate data from this project using a graphene meso-sponge cathode and data from the literature, respectively. Reprinted with permission from [80]. Copyright 2022 Elsevier. (e) Energy density plotted against specific energy. The red cross and blue crosses indicate data from this project and from the literature, respectively. Reprinted with permission from Ref. 79. Copyright 2023 John Wiley and Sons



high gravimetric energy density of approximately  $500 \text{ Wh kg}^{-1}$ , surpassing that of conventional lithium-ion batteries. Recognizing that cycle performance degradation is primarily caused by (1) the high decomposition overpotential of  $\text{Li}_2\text{O}_2$ , (2) cathode and electrolyte degradation due to reactive oxygen species, and (3) non-uniform lithium plating on the anode, we focused on analyzing the origins of high decomposition overpotentials, developing strategies for their reduction, and designing chemically stable cathodes and electrolytes. This study involved the quantitative evaluation of reactive oxygen species generated during charge and discharge, the assessment of  $\text{Li}_2\text{O}_2$  and electrolyte properties, and the development of design guidelines for cathode structures. Key achievements included the development of novel electrolytes incorporating dual-anion redox mediators, multifunctional electrolytes capable of quenching singlet oxygen and forming highly decomposable  $\text{Li}_2\text{O}_2$ , and

chemically stable, defect-free carbon cathodes with exceptional durability (Fig. 10 (b)–(d)) [74–76]. Additionally, we investigated battery reaction mechanisms using multiple advanced analytical techniques [77]. By integrating these technological advancements and fundamental insights, we achieved a world-record cycle performance at a gravimetric energy density of approximately  $500 \text{ Wh kg}^{-1}$  (Fig. 10(e)) [78, 79].

## 8 Mg metal battery

Mg metal is a promising anode material due to its high theoretical capacity ( $2205 \text{ mA h g}^{-1}$ ), low electrochemical potential ( $-2.38 \text{ V}$  vs. SHE), and non-dendritic deposition behavior during electrodeposition [81, 82]. However, despite these advantages, rechargeable Mg batteries have

not yet reached practical application, primarily due to the lack of suitable cathode materials and electrolytes. Therefore, advancing these components is crucial for the development of practical Mg battery systems.

Oxide-based cathode materials operating in the 2–3 V range offer higher energy density than traditional 1 V-class Chevrel-phase compounds [81]. However, their development has been limited by sluggish reaction kinetics. To address this, we hypothesized that increasing the operating temperature would enhance Mg ion diffusion within oxide lattices. This approach led to the discovery that several spinel-type oxides (e.g.,  $\text{MgCo}_2\text{O}_4$ ,  $\text{MgMn}_2\text{O}_4$ ,  $\text{MgFe}_2\text{O}_4$ ) exhibited substantial Mg insertion at 150 °C, accompanied by a phase transformation into a rocksalt structure (Fig. 11) [83].

To enhance the reversibility of the spinel-to-rocksalt phase transition, we systematically investigated the properties of derivative materials (e.g.,  $\text{ZnCo}_2\text{O}_4$ ,  $\text{ZnFe}_2\text{O}_4$ ). Our findings revealed that Zn ions, which preferentially occupy tetrahedral sites, facilitated the reverse transition from the rocksalt to spinel phase (Fig. 12a) [84]. Additionally, we examined the phase stability and the feasibility of Mg insertion and extraction in Mn-based oxides, including various  $\text{MnO}_2$  polymorphs [85, 86]. Notably, spinel-structured  $\lambda\text{-MnO}_2$ , although thermodynamically unstable, exhibited a

higher Mg insertion potential than tunnel-structured  $\alpha\text{-MnO}_2$  (Fig. 12b) [86].

Building on these insights, we developed a  $\text{ZnMnO}_3$  cathode, conceptualized as a ZnO-stabilized  $\lambda\text{-MnO}_2$  [87]. This material exhibited excellent cyclability ( $> 100$  cycles), moderate capacity ( $\sim 100 \text{ mA h g}^{-1}$ ), and an operating voltage range of 2–3 V at 150 °C (Fig. 13) [88]. Structural characterization revealed that  $\text{ZnMnO}_3$  adopted a defective spinel structure with cation deficiencies at the octahedral 16d sites. These defects created additional pathways and sites for Mg migration and accommodation, enabling stable single-phase reactions while suppressing the formation of an inert rocksalt phase [88].

Compared with other reported long-life cathode materials [81, 89, 90], this defect spinel-type material has a superior electrode potential (Fig. 14) [91]. Furthermore, the theoretical capacity is over 300 mAh g<sup>-1</sup> if the reaction to form a rocksalt phase is included. A current limitation is compatibility with other parts when constructing full cells. The ionic liquid electrolyte used here makes passivation of the Mg-metal anode, decreasing the cell voltage [92]. In addition, the operating temperature remains a significant challenge. Proposed strategies include using ultrasmall particles [93], high-entropy oxides [94], and alkali cation co-intercalation [95]. Another promising approach involves sulfur-based

**Fig. 11** Schematic illustration showing the intercalation and push-out process in spinel oxide cathode materials. The insertion of Mg ions into the 16c octahedral site induces the migration of the cations located at the tetrahedral 8a site to the adjacent octahedral 16c site, resulting in the transformation into a rocksalt phase. Reproduced with permission from Ref. 83. Copyright 2015 The Authors

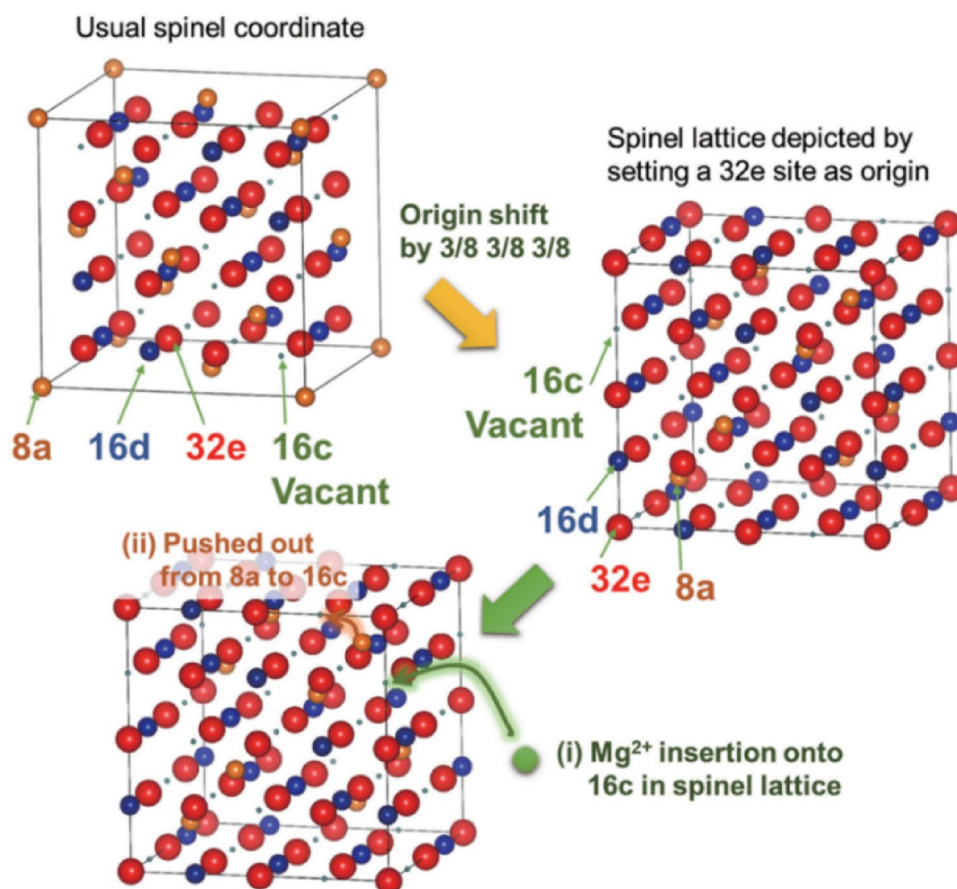




**Fig. 12** (a) Schematic diagram showing the spinel–rocksalt transition in Zn-based spinel oxides. Zn ions that prefer the tetrahedral environment accelerate the inverse rocksalt-to-spinel transition in the charging process. Reproduced with permission from Ref 84. Copyright 2019 The Royal Society of Chemistry. (b) Ab initio calculation for comparing the Mg insertion potentials in various MnO<sub>2</sub> polymorphs. Spinel-structured  $\lambda$ -MnO<sub>2</sub> provides the highest potential among them, while its structural instability is a problem in practical use. Reproduced with permission from Ref. 86. Copyright 2021 American Chemical Society

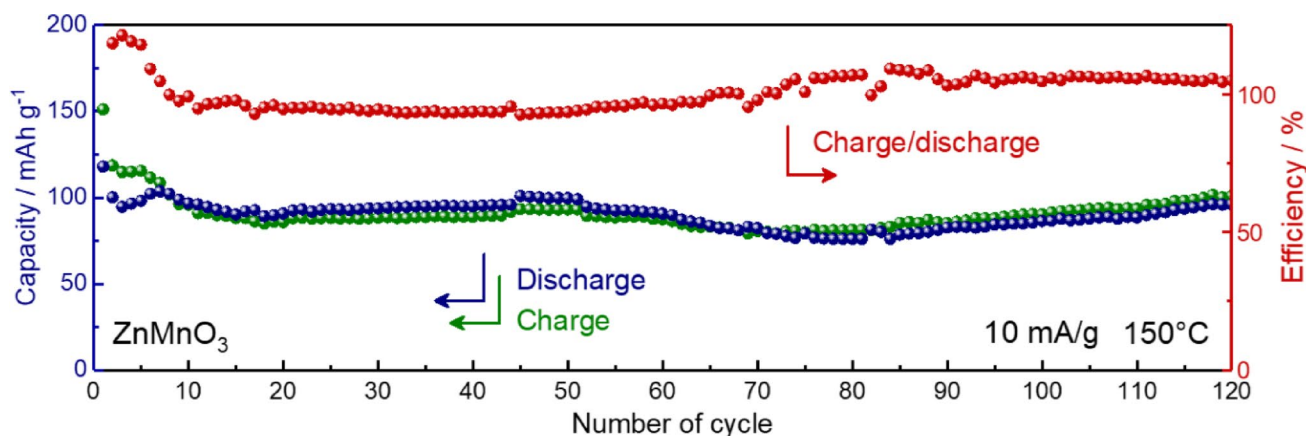
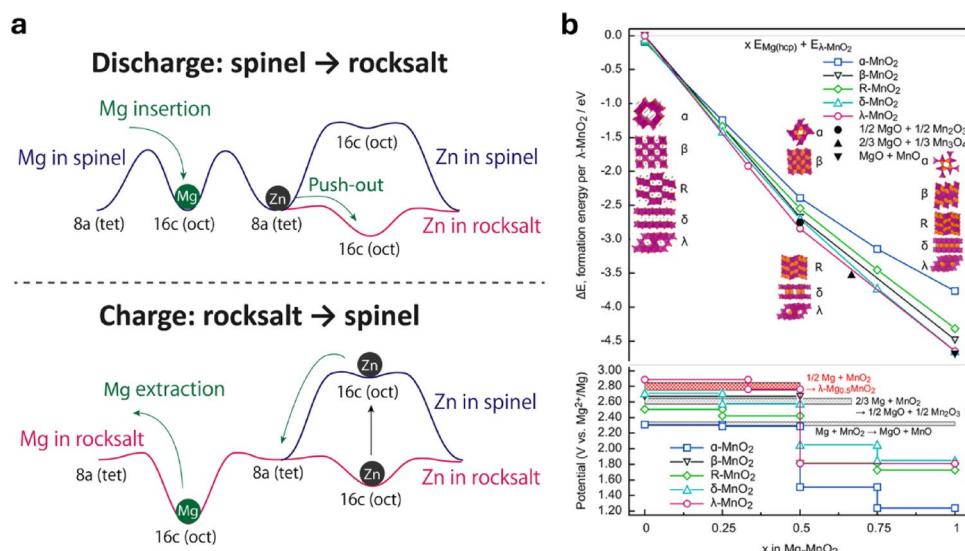


**Fig. 13** Long-life cycling performance of the defect-spinel ZnMnO<sub>3</sub> cathode material. In contrast to the rapid capacity fading in stoichiometric spinel oxides such as MgCo<sub>2</sub>O<sub>4</sub> and MgMn<sub>2</sub>O<sub>4</sub>, the defect spi-

nel ZnMnO<sub>3</sub> exhibited highly stable charge/discharge over 100 cycles at an elevated temperature of 150 °C. Reproduced with permission from Ref. 88. Copyright 2021 The Authors

materials, which offer high capacity and rate performance potential [96].

Electrolytes play a crucial role in battery performance. In metal anode-based systems, they must enable highly efficient and reversible metal plating and stripping, ideally achieving Coulombic efficiencies above 99.95% for practical applications. However, few electrolyte formulations—comprising solvents and conductive salts—are compatible with the highly reactive Mg metal [97, 98]. Electrolytes optimized for lithium-ion batteries often impair Mg plating/stripping reversibility due to severe passivation caused by unavoidable interfacial reactions [97, 99].

To address these limitations, developing passivation-free, highly efficient electrolytes is essential. Since the introduction of the first Mg battery prototype utilizing a highly corrosive alkylhaloaluminate-based electrolyte [81], significant research has focused on discovering more effective electrolyte systems. Weakly coordinated anion (WCA)-based

electrolytes have emerged as promising candidates for next-generation Mg batteries [100–102].

Among WCAs, boron- and aluminum-centered ate complex-based WCAs have attracted particular interest due to their structural tunability [101–104]. Their electrochemical performance depends strongly on ligand structure. Through systematic studies examining ligand structures, central elements, solvent selection, and salt concentrations, we identified an aluminate-based WCA with 1,1,1,3,3,3-hexafluoro-isopropoxy ligands ([Al(HFIP)<sub>4</sub>]<sup>-</sup>) in diglyme (G2) solvent that demonstrated exceptional electrochemical performance [105, 106].

This optimized electrolyte outperformed its borate-based counterpart ([B(HFIP)<sub>4</sub>]<sup>-</sup>) and conventional bis(trifluoromethanesulfonyl)amide ([TFSA]<sup>-</sup>)-based electrolytes, as shown in Fig. 15 [105, 106]. Galvanostatic Mg plating/stripping cycling tests confirmed its superior performance, achieving Coulombic efficiencies exceeding

**Fig. 14** Comparison of potential and capacity of the selected cathode materials in rechargeable Mg batteries. The advantage of the defect spinel  $\text{ZnMnO}_3$  compared with the other reported long-life cathode materials is its high electrode potential, whereas the practical capacity is limited. The dashed lines indicate the energy densities of rechargeable Mg batteries coupling the high-capacity Mg metal anode and the cathodes on the map. The energy density of a conventional  $\text{LiCo}_2\text{O}_4/\text{C}$  cell is also shown for comparison. Reproduced with permission from Ref. 91. Copyright 2023 Elsevier B.V

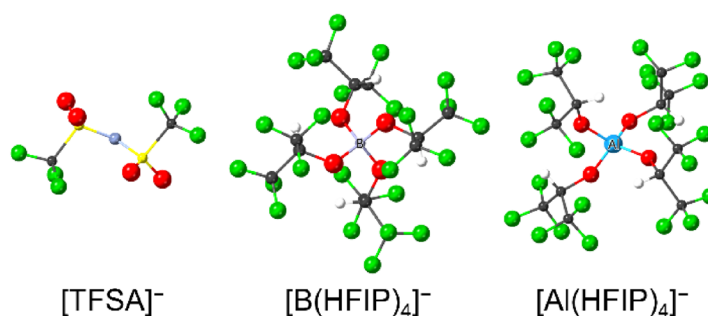
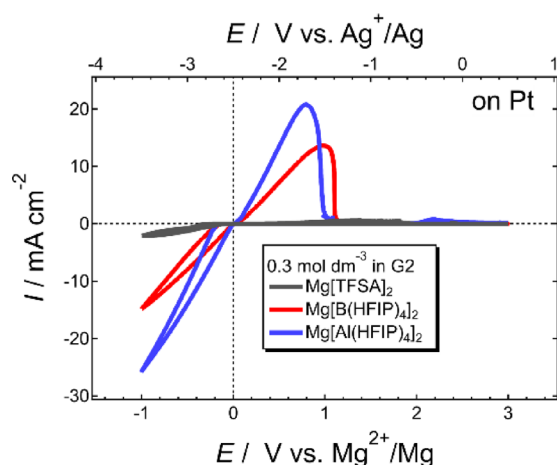
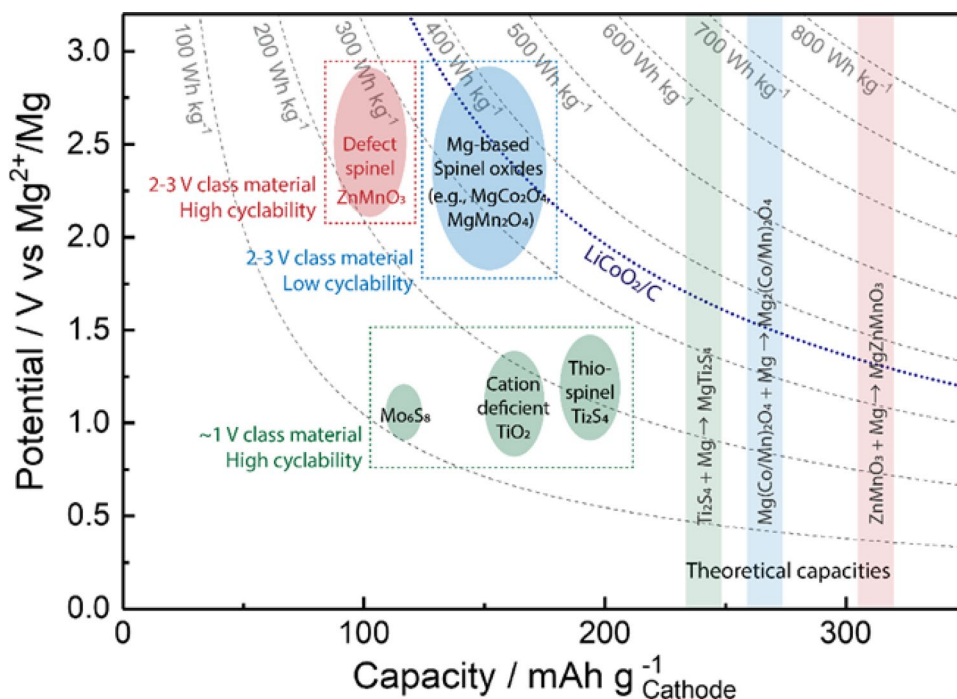


**Fig. 15** Cyclic voltammetry profiles of representative Mg battery electrolytes recorded on a Pt working electrode at 30 °C. The profiles of  $\text{Mg}[\text{Z}(\text{HFIP})_4]_2$  ( $\text{Z} = \text{B}, \text{Al}$ ) are reproduced with permission from Refs.

105 (Copyright 2020 American Chemical Society) and 106 (Copyright 2021 The Royal Society of Chemistry)

99.5% over 250 cycles (Fig. 16) [106]. To the best of our knowledge, this represents one of the highest-performing halide-free Mg battery electrolytes reported to date. Battery cycling tests with various cathode materials further demonstrated the superior compatibility of this electrolyte formulation [107], though potential side reactions require careful consideration [108]. Due to its exceptional properties, this electrolyte has been adopted as a standard in national battery projects in Japan and Germany. The successful development of this electrolyte marks a significant step toward realizing high-energy-density Mg batteries.

## 9 Li metal battery

Lithium metal anodes are used in Li-sulfur, Li-air, Li-metal, and all-solid-state Li-metal batteries. However, their low cyclability limits their application in next-generation batteries. Extensive research has been conducted to understand the degradation mechanisms of lithium metal during cycling. Lithium metal readily reacts with electrolytes, forming a solid electrolyte interphase (SEI), as shown in Fig. 17 [109]. The chemical composition of SEI has been analyzed using FTIR, XPS, and other techniques [110–112]. These analyses have revealed that SEI composition depends on the electrolyte type, electrolyte additives, and charge-discharge

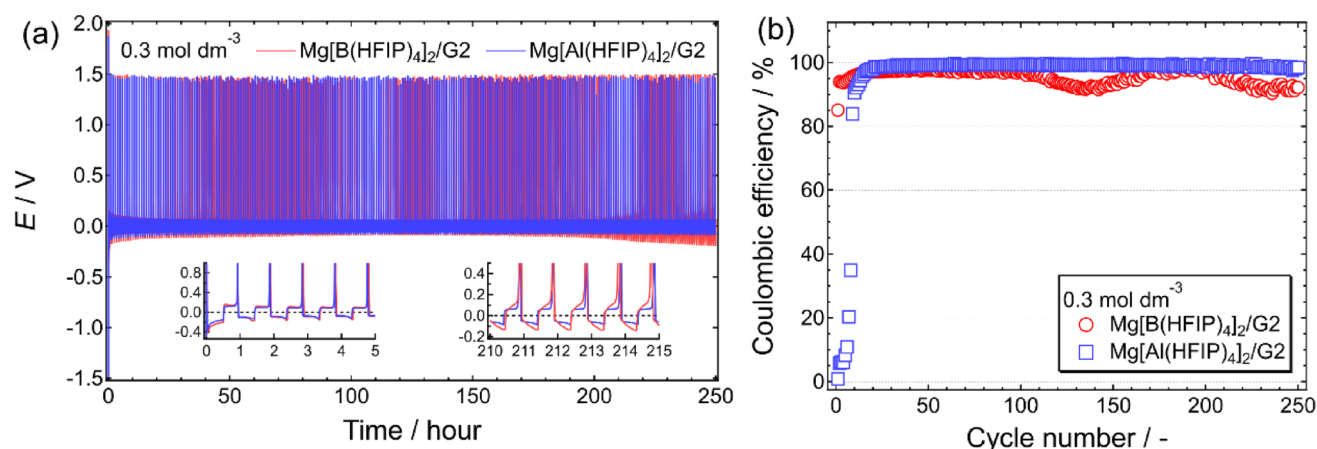


**Fig. 16** (a) Galvanostatic cycling profiles and (b) corresponding Coulombic efficiencies of  $[\text{Mg} \parallel \text{Cu}]$  asymmetric cells employing  $0.3 \text{ mol dm}^{-3} \text{ Mg}[\text{Z}(\text{HFIP})_4]_2/\text{G2}$  electrolytes, measured at a current density of

$0.5 \text{ mA cm}^{-2}$  and a temperature of  $30^\circ \text{C}$ . Reproduced with permission from Ref. [106]. Copyright 2022 American Chemical Society

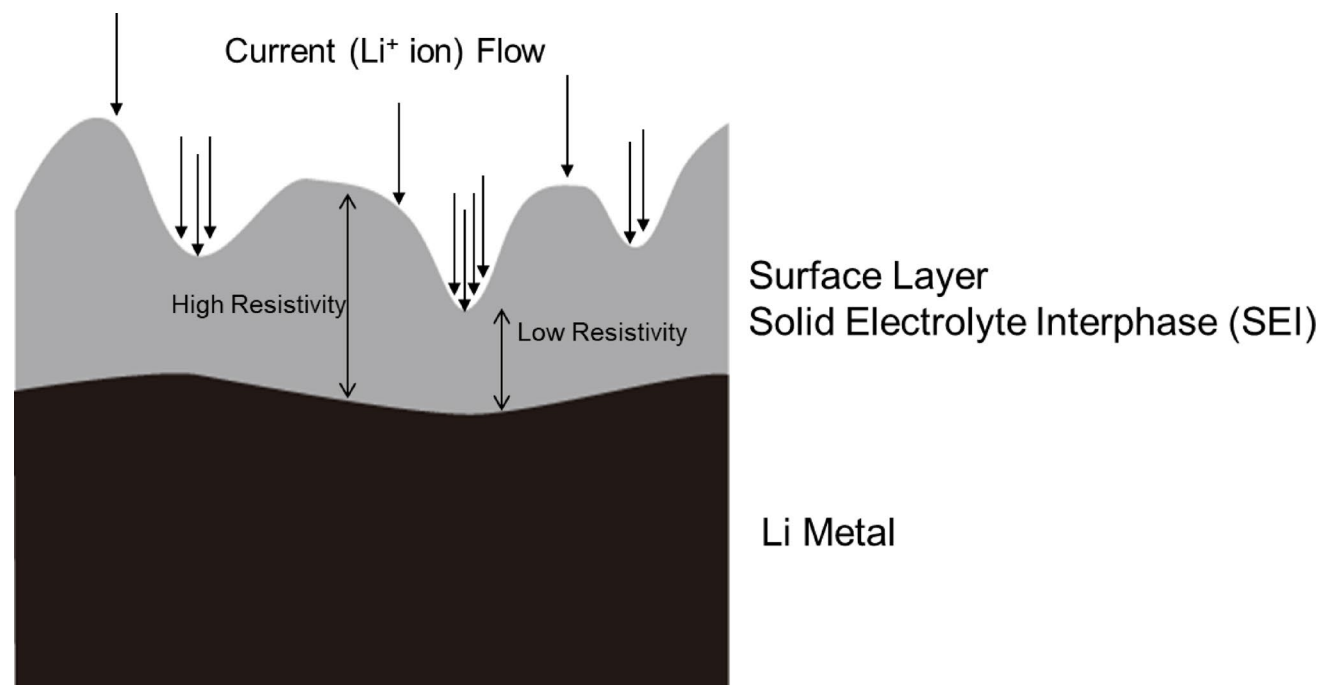


**Fig. 17** Schematic illustration of the SEI layer on a Li metal surface. The non-uniform SEI layer leads to a distribution of  $\text{Li}^+$  ion flux, and this non-uniformity enhances localized Li electrodeposition and dissolution.

conditions. Additionally, the uniformity of SEI thickness is strongly influenced by these factors. Poor SEI uniformity leads to uneven current distribution within the cell, significantly affecting the cycle life of the lithium metal anode. Non-uniform current distribution leads to a localized concentration of  $\text{Li}^+$  ion flow on the lithium metal surface. The morphology of lithium metal is directly influenced by the current distribution near its surface. Concentrated current flow promotes the formation of lithium metal with a dendritic morphology [113]. These dendrites have a high surface area, intensifying chemical reactions between lithium

metal and the electrolyte. The chemical reduction of the electrolyte produces byproducts such as  $\text{LiF}$ ,  $\text{Li}_2\text{CO}_3$ ,  $\text{Li}_2\text{O}$ , and Li alkyl carbonate (or other organics) [114]. These reaction products further exacerbate non-uniform current distribution on the lithium metal anode surface. To achieve long cycle life in lithium metal anodes, maintaining a uniform current distribution near the lithium metal surface is essential. A uniform  $\text{Li}^+$  ion flow distribution suppresses dendrite formation.

This project investigated two approaches to control current distribution near the lithium metal surface. The first

involved artificially modifying the SEI using additives or artificial SEI layers composed of  $\text{Li}^+$ -conductive polymers or gels. Li metal reacts with some chemical species at Li metal surface to form SEI. Artificial SEI will be designed to get uniform  $\text{Li}^+$  flux to Li metal surface and prevent the undesirable side reaction between electrodeposited Li metal and electrolytes. In addition, artificial SEI needs mechanical toughness because Li metal repeats large volume change during charge and discharge cycles [115, 116]. Regarding design of artificial SEI, we have succeeded in forming a gel with hydrogen-bond on Li metal surface by taking over other projects [117, 118]. On the other hand, in terms of SEI analysis technology, a method using an ultramicroelectrode as model electrode was established, and we have reported the identification technique of lithium compounds in SEI layer by cryo-STEM-EELS [119].

The second focused on developing a novel separator. Figure 18(a) presents an SEM image of a polyimide separator with an inverse opal (IOP) structure [120, 121]. This separator significantly improved current uniformity at the interface between the separator and the lithium metal surface. The IOP separator was synthesized using a templating method. Mono-dispersed silica or polymer beads, with particle sizes of a few hundred nanometers, were used to prepare the opal-structured template sheet. A polyamic acid solution in dimethylacetamide was injected into the voids of the opal-structured template composed of microbeads. After polymerization at 300 °C, the template beads were removed using an HF aqueous solution for silica beads or a heating process below 300 °C for polymer beads. The IOP separator effectively controlled current distribution, ensuring a more uniform  $\text{Li}^+$  ion flow at the lithium metal surface. Figure 18(b) presents an SEM image of lithium metal after 100 cycles in a Li metal/IOP separator/electrolyte/Li metal symmetric cell with ethylene carbonate/1.0 mol  $\text{dm}^{-3}$   $\text{LiPF}_6$

electrolyte. The IOP separator suppressed lithium dendrite formation due to its highly uniform  $\text{Li}^+$  ion flow distribution and SEI stabilization. The discharge and charge cycle performance of the cell with NMC cathode, Li metal anode and IOP separator was improved, but the cycle number was less than 200 cycles. Figure 19 displays the discharge and charge curves of a lithium metal battery with a  $\text{LiNi}_{0.5}\text{Mn}_{0.2}\text{Co}_{0.3}\text{O}_2$  cathode and a newly developed electrolyte. The combination of the IOP separator and the new electrolyte resulted in improved cycle performance. The polyimide-based IOP separator exhibited superior wettability compared to conventional polyolefin separators, making it suitable for highly concentrated electrolytes. While many studies employed thick glass separators for such electrolytes, the IOP separator provided an effective alternative. Additionally, the highly concentrated electrolyte demonstrated lower reactivity with lithium metal, further enhancing cycle performance [122, 123]. In fact, the discharge and charge curves were obtained by using 3.0 mol  $\text{dm}^{-3}$  LiFSI/EMI-FSI ionic liquid which cannot be used in the cell with polyolefin separator owing to low wettability of this electrolyte to polyolefin separator. The cycle number of this small lithium metal battery was more than 500 cycles and its estimated energy density of cell was more than 400  $\text{Wh kg}^{-1}$ . As described above, the cycle performance of lithium metal battery strongly depends on a reactivity of electrolyte with lithium metal anode. This ionic liquid can provide very low reactivity, leading to less consumption of electrolyte. A similar behavior was also observed by using dimethyl carbonate/5.5 mol  $\text{dm}^{-3}$  LiFSI electrolyte. This electrolyte also has a less reactivity with lithium metal [122]. In conclusion, lithium metal batteries can be realized through the use of a less reactive electrolyte and the IOP separator. The development of new electrolytes and improvement of IOP separator has been continued in new project in Japan. These new materials have not only

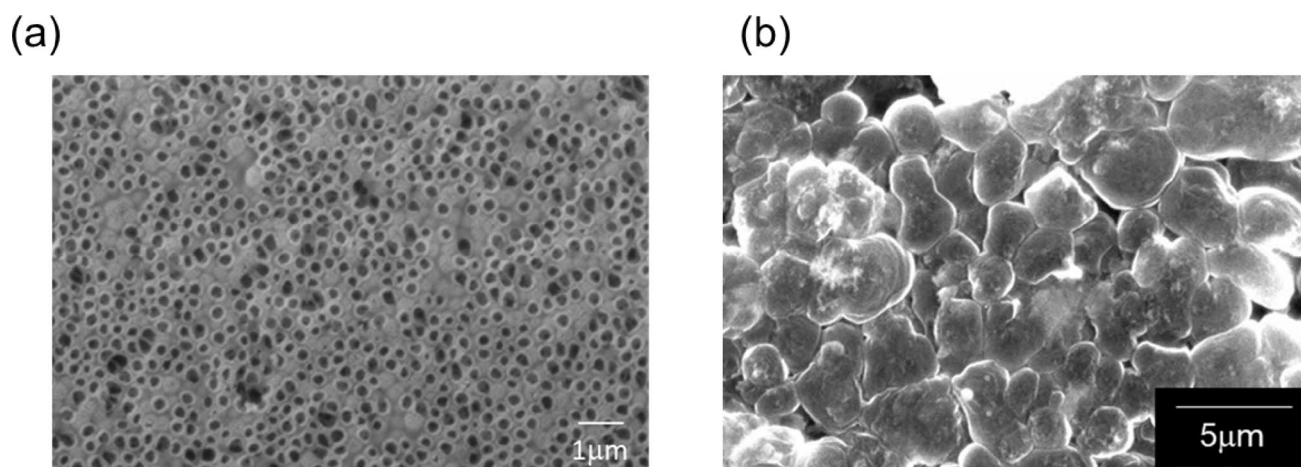
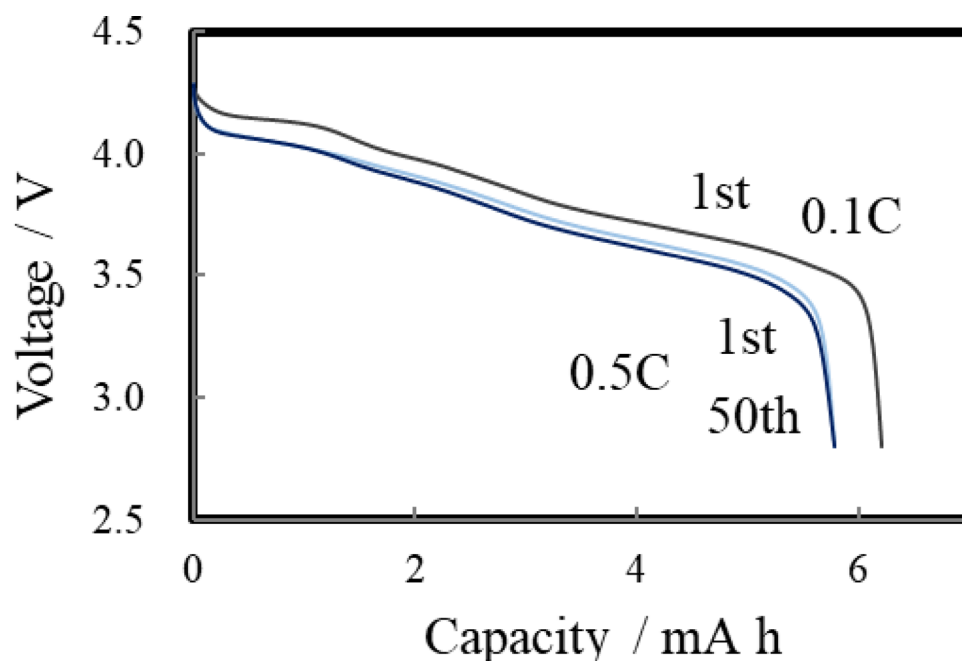


**Fig. 18** SEM images of (a) an IOP separator and (b) a Li metal surface after 100 cycles in ethylene carbonate containing 1 mol  $\text{dm}^{-3}$   $\text{LiPF}_6$  at 15.89 mA for 30 min (7.945 mAh)



**Fig. 19** Discharge and charge curves of an NMC523/Li metal full cell with newly developed electrolyte at room temperature, cycled at 0.1 C for the initial activation cycle followed by 0.5 C for subsequent cycling



applied to lithium metal battery, but also to lithium ion battery and other next generation batteries. At least, Li sulfur battery and Li air battery need a reversible Li metal anode. In these batteries, different types of electrolytes may be used to keep cathode reactions. Therefore, further development of new electrolytes is a key issue for these next-generation batteries

## 10 Summary

In the ALCA-SPRING project, six types of next-generation batteries were developed. Each of these battery systems is attracting worldwide attention, and we believe that the knowledge of this project will make a significant contribution. Among them, ASSBs with sulfide electrolytes and lithium metal batteries have the potential for commercialization in the near future. However, ASSBs with sulfide electrolytes has challenge to make it larger, and lithium metal battery remains problem with regard to cycle life performance beyond 1,000 cycles. Although lithium-sulfur batteries may also become commercially available, it is necessary to improve the cycle life. Mg metal batteries, ASSBs with oxide electrolytes, and lithium-air batteries still require further fundamental research. It became much clear that it was necessary to find positive active materials that would allow  $\text{Mg}^{2+}$  ion to move fast. For ASSBs with oxide electrolytes, although the operation of the small cells has been confirmed, when the cell size is larger, issues such as the bondability of each component become apparent. For Li-air batteries, it became clear that designing the electrodes based on an understanding of the reaction mechanism of the

air electrode is indispensable. Currently, none of these next-generation batteries have been commercialized. In October 2023, Japan launched a new project known as Green Technology of Excellence (GteX) program. This initiative encompasses not only rechargeable battery research but also studies on hydrogen production via electrolysis and biomanufacturing. The rechargeable battery research segment, a crucial area of the project, focuses on seven types of next-generation batteries as well as advanced lithium-ion batteries. Specifically, ASSBs, lithium-sulfur batteries, lithium-air batteries, and magnesium metal batteries are included. Within the next decade, some of these next-generation batteries are expected to be commercialized. Lithium-ion batteries are also part of the GteX project, highlighting their continued importance in practical applications. Significant advancements in lithium-ion battery technology are anticipated as part of this initiative.

**Acknowledgements** This work was supported by ALCA-SPRING project funded by the Japan Science and Technology Agency (grant number JPMJAL1301).

## Declarations

**Conflict of interest** The authors declare that they have no known competing financial interests or personal relationships that could have appeared to influence the work reported in this paper. On behalf of all authors, the corresponding author states that there is no conflict of interest.

**Open Access** This article is licensed under a Creative Commons Attribution 4.0 International License, which permits use, sharing, adaptation, distribution and reproduction in any medium or format, as long as you give appropriate credit to the original author(s) and the source, provide a link to the Creative Commons licence, and indicate



if changes were made. The images or other third party material in this article are included in the article's Creative Commons licence, unless indicated otherwise in a credit line to the material. If material is not included in the article's Creative Commons licence and your intended use is not permitted by statutory regulation or exceeds the permitted use, you will need to obtain permission directly from the copyright holder. To view a copy of this licence, visit <http://creativecommons.org/licenses/by/4.0/>.

## References

- K. Kanamura, in, *Electrochemical Science for a Sustainable Society, A Tribute to John O' M Bockris, Large-Scale Batteries for Green Energy Society*, ed by K. UosakiSpringer, Dordrecht, (2017) 175
- J. Liu, J.-G. Zhang, Z. Yang, J.P. Lemmon, C. Imhoff, G.L. Graff, L. Li, J. Hu, C. Wang, J. Xiao, G. Xia, V.V. Viswanathan, S. Bakaran, V. Sprenkle, X. Li, Y. Shao, B. Schwenzer, *Adv. Funct. Mater.* **23**, 929 (2013)
- <https://www.ipcei-batteries.eu/technology-fields>. Accessed 9 January 2025
- <https://www.solstice-battery.eu/>
- [https://www.acc-emotion.com/sites/default/files/media/files/ACC\\_Press\\_Kit\\_BBD\\_EN\\_FINAL\\_acc-emotion\\_0.pdf](https://www.acc-emotion.com/sites/default/files/media/files/ACC_Press_Kit_BBD_EN_FINAL_acc-emotion_0.pdf). Accessed 9 January 2025
- <https://www.faraday.ac.uk/faraday-battery-challenge/>. Accessed 9 January 2025
- <https://www.pnnl.gov/innovation-center-battery500-consortium>. Accessed 9 January 2025
- K. Kanamura, Y. Yamada, *Next Generation Batteries* (Springer, Dordrecht, 2021), pp. 3–13
- X. Zhang, H. Jia, Y. Xu, L. Zou, M.H. Engelhard, B.E. Matthews, C. Wang, J.-G. Zhang, W. Xu, *J. Power Sources Adv.* **5**, 10024 (2020)
- Japan, - Countries & Regions - IEA. <https://www.iea.org/countries/japan/energy-mix>. Accessed 9 January 2025
- S. Nyamathulla, C. Dhanamjayulu, *J. Energy Storage* **86** Part. A 111179 (2024)
- J. Janek, W.G. Zeier, *Nat. Energy* **8**, 230 (2023)
- A. Banerjee, X. Wang, C. Fang, E.A. Wu, Y.S. Meng, *Chem. Rev.* **120**, 6878 (2020)
- T. Schmaltz, F. Hartmann, T. Wicke, L. Weymann, C. Neef, J. Janek, *Adv. Energy Mater.* **13**, 2301886 (2023)
- Y. Li, S. Song, H. Kim, K. Nomoto, H. Kim, X. Sun, S. Hori, K. Suzuki, N. Matsui, M. Hirayama, T. Mizoguchi, T. Saito, T. Kamiyama, R. Kanno, *Science* **281**, 50 (2023)
- A. Sakuda, A. Hayashi, M. Tatsumisago, *Sci. Rep.* **3**, 2261 (2013)
- T. Shigedomi, Y. Fujita, T. Kishi, K. Motohashi, H. Tsukasaki, H. Nakajima, S. Mori, M. Tatsumisago, A. Sakuda, A. Hayashi, *Chem. Mater.* **34**, 9745 (2022)
- T. Krauskopf, F.H. Richter, W.G. Zeier, J. Janek, *Chem. Rev.* **120**, 7745 (2020)
- A. Kato, M. Nose, M. Yamamoto, A. Sakuda, A. Hayashi, M. Tatsumisago, *J. Ceram. Soc. Jpn.* **126**, 719 (2018)
- M. Suyama, A. Kato, A. Sakuda, A. Hayashi, M. Tatsumisago, *Electrochim. Acta* **286**, 1158 (2018)
- T. Asakura, T. Inaoka, C. Hotehama, H. Kowada, K. Motohashi, A. Sakuda, M. Tatsumisago, A. Hayashi, *ACS Appl. Mater. Interfaces* **15**, 31403 (2023)
- T. Inaoka, T. Asakura, M. Otoyama, K. Motohashi, A. Sakuda, M. Tatsumisago, A. Hayashi, *J. Phys. Chem. C* **127**, 10453 (2023)
- J. Akimoto, T. Akao, K. Kataoka, *Small* **19**, 2301617 (2023)
- N. Hamao, K. Hamamoto, N. Taguchi, S. Tanaka, J. Akimoto, *Solid State Ionics* **357**, 115460 (2020)
- K. Watanabe, A. Tashiro, Y. Ichinose, S. Takeno, K. Suematsu, K. Mitsuishi, K. Shimanoe, *J. Ceram. Soc. Jpn.* **130**, 416 (2022)
- T. Okumura, T. Takeuchi, H. Kobayashi, *ACS Appl. Energy Mater.* **4**, 30 (2021)
- N. Hayashi, K. Watanabe, K. Shimanoe, *J. Mater. Chem. A* **12**, 5269 (2024)
- Y. Ren, Y. Shen, Y. Lin, C.-W. Nan, *Electrochem. Commun.* **57**, 27 (2015)
- X. Ma, Y. Xu, *Electrochim. Acta* **441**, 141789 (2023)
- L. Cheng, M. Liu, A. Mehta, H. Xin, F. Lin, K. Persson, G. Chen, E.J. Crumlin, M. Doeff, *ACS Appl. Energy Mater.* **1**, 7244 (2018)
- T. Ohnishi, I. Sakaguchi, K. Takada, *ACS Appl. Energy Mater.* **7**, 5321 (2024)
- H. Aono, E. Sugimoto, Y. Sadaoka, N. Imanaka, G. Adachi, *J. Electrochem. Soc.* **137**, 1023 (1990)
- Y. Inaguma, C. Liqun, M. Itoh, T. Nakamura, T. Uchida, H. Ikuta, M. Wakihara, *Solid State Commun.* **86**, 689 (1993)
- Y. Li, J.-T. Han, C.-A. Wang, H. Xie, J.B. Goodenough, *J. Mater. Chem.* **22**, 15357 (2012)
- J. Kim, J. Kim, M. Avdeev, H. Yun, S.-J. Kim, *J. Mater. Chem. A* **6**, 22478 (2018)
- A. Aimi, H. Onodera, Y. Shimonishi, K. Fujimoto, S. Yoshida, *Chem. Mater.* **36**, 3717 (2024)
- P.G. Bruce, S.A. Freunberger, L.J. Hardwick, J.-M. Tarascon, *Nat. Mater.* **11**, 19 (2011)
- A. Manthiram, Y. Fu, Y.-S. Su, *Acc. Chem. Res.* **46**, 1125 (2013)
- X. Ji, K.T. Lee, L.F. Nazar, *Nat. Mater.* **8**, 500 (2009)
- N. Tachikawa, K. Yamauchi, E. Takashima, J.-W. Park, K. Dokko, M. Watanabe, *Chem. Commun. (Camb)* **47**, 8157 (2011)
- K. Dokko, N. Tachikawa, K. Yamauchi, M. Tsuchiya, A. Yamazaki, E. Takashima, J.-W. Park, K. Ueno, S. Seki, N. Serizawa, M. Watanabe, *J. Electrochem. Soc.* **160**, A1304 (2013)
- A. Nakanishi, K. Ueno, D. Watanabe, Y. Ugata, Y. Matsumae, J. Liu, M.L. Thomas, K. Dokko, M. Watanabe, *J. Phys. Chem. C* **123**, 14229 (2019)
- M. Yanagi, K. Ueno, A. Ando, S. Li, Y. Matsumae, J. Liu, K. Dokko, M. Watanabe, *J. Electrochem. Soc.* **167**, 070531 (2020)
- Y. Ugata, R. Tataru, T. Mandai, K. Ueno, M. Watanabe, K. Dokko, *ACS Appl. Energy Mater.* **4**, 1851 (2021)
- H. Asano, J. Liu, K. Ueno, K. Dokko, T. Kojima, N. Takeichi, T. Miyuki, Y. Yamakawa, M. Watanabe, *J. Power Sources* **554**, 232323 (2023)
- J. Liu, T. Kaneko, J.-Y. Ock, S. Kondou, K. Ueno, K. Dokko, K. Sodeyama, M. Watanabe, *J. Phys. Chem. C* **127**, 5689 (2023)
- J. Liu, S. Li, N. Nomura, K. Ueno, K. Dokko, M. Watanabe, *ACS Appl. Mater. Interfaces* **16**, 8570 (2024)
- T. Ishikawa, S. Haga, K. Shigenobu, T. Sudoh, S. Tsuzuki, W. Shinoda, K. Dokko, M. Watanabe, K. Ueno, *Faraday Discuss.* **253**, 385 (2024)
- J.-W. Park, K. Ueno, N. Tachikawa, K. Dokko, M. Watanabe, *J. Phys. Chem. C* **117**, 20531 (2013)
- K. Ueno, J.-W. Park, A. Yamazaki, T. Mandai, N. Tachikawa, K. Dokko, M. Watanabe, *J. Phys. Chem. C* **117**, 20509 (2013)
- K. Dokko, D. Watanabe, Y. Ugata, M.L. Thomas, S. Tsuzuki, W. Shinoda, K. Hashimoto, K. Ueno, Y. Umebayashi, M. Watanabe, *J. Phys. Chem. B* **122**, 10736 (2018)
- K. Shigenobu, K. Dokko, M. Watanabe, K. Ueno, *Phys. Chem. Chem. Phys.* **22**, 15214 (2020)
- S. Li, S. Ishikawa, J. Liu, K. Ueno, K. Dokko, G. Inoue, M. Watanabe, *Batteries Supercaps* **5**, e202100409 (2022)
- J. Liu, S. Li, M. Marium, B. Wang, K. Ueno, K. Dokko, M. Watanabe, *Sustainable Energy Fuels* **5**, 1821 (2021)
- Y. Ugata, K. Shigenobu, R. Tataru, K. Ueno, M. Watanabe, K. Dokko, *Phys. Chem. Chem. Phys.* **23**, 21419 (2021)

56. S. Li, Z. Chen, K. Yamamoto, T. Watanabe, Y. Uchimoto, Y. Mori, G. Inoue, K. Ohuchi, S. Inagaki, K. Ueno, K. Dokko, M. Watanabe, *Adv. Mater. Interfaces*. **11**, 2300864 (2023)
57. T. Takahashi, M. Yamagata, M. Ishikawa, *Prog Nat. Sci.* **25**, 612 (2015)
58. S. Usuki, S. Uchida, Y. Matsui, M. Yamagata, H. Hinago, M. Ishikawa, *Electrochemistry*. **85**, 650 (2017)
59. Y. Torii, Y. Matsui, K. Yamamoto, S. Uchida, S. Yamazaki, T. Watanabe, K. Nakanishi, T. Uchiyama, Y. Uchimoto, M. Ishikawa, *J. Phys. Chem. C* **127**, 15069 (2023)
60. S. Okabe, S. Uchida, Y. Matsui, M. Yamagata, M. Ishikawa, *Electrochemistry*. **85**, 671 (2017)
61. L. Yoshida, T. Hakari, Y. Matsui, M. Deguchi, H. Yamamoto, M. Inoue, M. Ishikawa, *J. Power Sources*. **624**, 235572 (2014)
62. T. Tonoya, Y. Matsui, M. Ishikawa, *Electrochemistry*. **92**, 77007 (2024)
63. L. Yoshida, Y. Matsui, M. Deguchi, T. Hakari, M. Watanabe, M. Ishikawa, *ACS Appl. Mater. Interfaces*. **15**, 37467 (2023)
64. H.S. Kim, T.-G. Jeong, Y.-T. Kim, *J. Electrochem. Sci. Technol.* **7**, 228 (2016)
65. S. Dörfler, S. Walus, J. Locke, A. Fotouhi, D.J. Auger, N. Shateri, T. Abendroth, P. Härtel, H. Althues, S. Kaskel, *Energy Technol.* **8**, 2000694 (2020)
66. J.B. Robinson, K. Xi, R.V. Kumar, A.C. Ferrari, H. Au, M.M. Titirici, A.P. Puerto, A. Kucernak, S.D.S. Fitch, N.G. Araez, Z.L. Brown, M. Pasta, L. Furness, A.J. Kibler, D.A. Walsh, L.R. Johnson, C. Holc, G.N. Newton, N.R. Champness, F. Markoulidis, C. Crean, R.C.T. Slade, E.I. Andritsos, Q. Cai, S. Babar, T. Zhang, C. Lekakou, N. Kulkarni, A.J.E. Rettie, R. Jervis, M. Cornish, M. Marinescu, G. Offer, Z. Li, L. Bird, C.P. Grey, M. Chhowalla, D.D. Lecce, R.E. Owen, T.S. Miller, D. J. L., S. Brett, Liatard, D. Ainsworth, P. R., Shearing, *J. Phys. Energy* **3**, 031501 (2021)
67. M. Shaibani, M.S. Mirshekarloo, R. Singh, C.D. Easton, M.C.D. Cooray, N. Eshraghi, T. Abendroth, S. Dörfler, H. Althues, S. Kaskel, A.F. Hollenkamp, M.R. Hill, M. Majumder, *Sci. Adv.* **6**, eaay2757 (2020)
68. Lyten Inc, <https://lyten.com/technology/3d-graphene/> (2025)
69. A. Manthiam, Y. Fu, S.-H. Chung, C. Zu, Y.-S. Su, *Chem. Rev.* **114**, 11751 (2014)
70. L.J. Hardwick, *Faraday Discuss.* **248**, 412 (2024)
71. G. Leverick, Y. Shao-Horn, *Adv. Energy Mater.* **13**, 2204094 (2023)
72. W.J. Kwak, N. Rosy, D. Sharon, C. Xia, H. Kim, L.R. Johnson, P.G. Bruce, L.F. Nazar, L.F.Y.K. Sun, A.A. Frimer, M. Noked, S.A. Freunberger, D. Aurbach, *Chem. Rev.* **120**, 6626 (2020)
73. T. Liu, J.P. Vivek, E.W. Zhao, J. Lei, N. Garcia-Araez, C.P. Grey, *Chem. Rev.* **120**, 6558 (2020)
74. X. Xin, K. Ito, Y. Kubo, *ACS Appl. Mater. Interfaces*. **9**, 25976 (2017)
75. K. Nishioka, M. Tanaka, H. Fujimoto, T. Amaya, S. Ogoshi, M. Tobisu, S. Nakanishi, *Angew Chem. Int. Ed.* **61**, e202112769 (2022)
76. K. Nishioka, M. Tanaka, T. Goto, R. Haas, A. Henss, S. Azuma, M. Saito, S. Matsuda, W. Yu, H. Nishihara, H. Fujimoto, M. Tobisu, Y. Mukouyama, S. Nakanishi, *ACS Appl. Mater. Interfaces*. **16**, 46259 (2024)
77. A. Dutta, K. Ito, A. Nomura, Y. Kubo, *Adv. Sci.* **7**, 2001660 (2020)
78. S. Matsuda, M. Ono, S. Yamaguchi, K. Uosaki, *Mater. Horiz.* **9**, 856 (2022)
79. S. Matsuda, M. Ono, H. Asahina, S. Kimura, E. Mizuki, E. Yasukawa, S. Yamaguchi, Y. Kubo, K. Uosaki, *Adv. Energy Mater.* **13**, 2203062 (2023)
80. Z. Liang, W. Wang, Y.-C. Lu, *Joule*. **6**, 2458 (2022)
81. D. Aurbach, Z. Lu, A. Schechter, Y. Gofer, H. Gizbar, R. Turgeman, Y. Cohen, M. Moshkovich, E. Levi, *Nature*. **407**, 724 (2000)
82. M. Matsui, *J. Power Sources*. **196**, 7048 (2011)
83. S. Okamoto, T. Ichitsubo, T. Kawaguchi, Y. Kumagai, F. Oba, S. Yagi, K. Shimokawa, N. Goto, T. Doi, E. Matsubara, *Adv. Sci.* **2**, 1500072 (2015)
84. K. Shimokawa, T. Atsumi, M. Harada, R.E. Ward, M. Nakayama, Y. Kumagai, F. Oba, N.L. Okamoto, K. Kanamura, T. Ichitsubo, *J. Mater. Chem. A* **7**, 12225 (2019)
85. T. Hatakeyama, N.L. Okamoto, K. Shimokawa, H. Li, A. Nakao, Y. Uchimoto, H. Tanimura, T. Kawaguchi, T. Ichitsubo, *Phys. Chem. Chem. Phys.* **21**, 23749 (2019)
86. T. Hatakeyama, H. Li, N.L. Okamoto, K. Shimokawa, T. Kawaguchi, H. Tanimura, S. Imashuku, M. Fichtner, T. Ichitsubo, *Chem. Mater.* **33**, 6983 (2021)
87. X. Ye, K. Shimokawa, Y. Kezuka, T. Hatakeyama, H. Li, T. Ichitsubo, *J. Phys. Chem. C* **127**, 5210 (2023)
88. K. Shimokawa, T. Atsumi, N.L. Okamoto, T. Kawaguchi, S. Imashuku, K. Wagatsuma, M. Nakayama, K. Kanamura, T. Ichitsubo, *Adv. Mater.* **33**, e2007539 (2021)
89. T. Koketsu, J. Ma, B.J. Morgan, M. Body, C. Legein, W. Dachraoui, M. Giannini, A. Demortière, M. Salanne, F. Dardozie, H. Groult, O.J. Borkiewicz, K.W. Chapman, P. Strasser, D. Dambournet, *Nat. Mater.* **16**, 1142 (2017)
90. X. Sun, P. Bonnick, V. Duffort, M. Liu, Z. Rong, K.A. Persson, G. Ceder, L.F. Nazar, *Energy Environ. Sci.* **9**, 2273 (2016)
91. K. Shimokawa, T. Hatakeyama, H. Li, T. Ichitsubo, *Curr. Opin. Electrochem.* **38**, 101209 (2023)
92. K. Shimokawa, H. Matsumoto, T. Ichitsubo, *J. Phys. Chem. Lett.* **9**, 4732 (2018)
93. H. Kobayashi, Y. Fukumi, H. Watanabe, R. Iimura, N. Nishimura, T. Mandai, Y. Tominaga, M. Nakayama, T. Ichitsubo, I. Honma, H. Imai, *ACS Nano*. **17**, 3135 (2023)
94. T. Kawaguchi, M. Yasuda, N. Nemoto, K. Shimokawa, H. Li, N.L. Okamoto, T. Ichitsubo, *J. Mater. Chem. A* **12**, 9088 (2024)
95. Y. Qi, H. Li, K. Shimokawa, X. Ye, T. Kawaguchi, T. Ichitsubo, *J. Phys. Chem. C* **127**, 21271 (2023)
96. K. Shimokawa, T. Furuhashi, T. Kawaguchi, W.-Y. Park, T. Wada, H. Matsumoto, H. Kato, T. Ichitsubo, *J. Mater. Chem. A* **9**, 16585 (2021)
97. T.D. Gregory, R.J. Hoffman, R.C. Winterton, *J. Electrochem. Soc.* **137**, 775 (1990)
98. T. Mandai, M. Yao, K. Sodeyama, A. Kagatsume, Y. Tateyama, H. Imai, *J. Phys. Chem. C* **127**, 10419 (2023)
99. I. Shterenberg, M. Salama, Y. Gofer, D. Aurbach, *Langmuir*. **33**, 9472 (2017)
100. O. Tutusaus, R. Mohtadi, T.S. Arthur, F. Mizuno, E.G. Nelson, Y.V. Sevryugina, *Angew Chem. Int. Ed. Engl.* **54**, 7900 (2015)
101. Z. Zhao-Karger, M.E.G. Bardaji, O. Fuhr, M. Fichtner, *J. Mater. Chem. A* **5**, 140815 (2017)
102. J.T. Herb, C.A. Nist-Lund, C.B. Arnold, *ACS Energy Lett.* **1**, 1205 (2016)
103. E.N. Keyzer, J. Lee, Z. Liu, A.D. Bond, D.S. Wright, C.P. Grey, *J. Mater. Chem. A* **7**, 2677 (2019)
104. S. Li, J. Zhang, S. Zhang, Q. Liu, H. Cheng, L. Fan, W. Zhang, X. Wang, Q. Wu, Y. Lu, *Nat. Energy*. **9**, 285 (2024)
105. T. Mandai, *ACS Appl. Mater. Interfaces*. **12**, 39135 (2020)
106. T. Mandai, Y. Youn, Y. Tateyama, *Mater. Adv.* **2**, 6283 (2021)
107. T. Pavčnik, M. Lozinšek, K. Pirnat, A. Vizintin, T. Mandai, D. Aurbach, R. Dominko, J. Bitenc, *ACS Appl. Mater. Interfaces*. **14**, 26766 (2022)
108. X. Ye, H. Li, T. Hatakeyama, H. Kobayashi, T. Mandai, N.L. Okamoto, T. Ichitsubo, *ACS Appl. Mater. Interfaces*. **14**, 56685 (2022)
109. K. Kanamura, *Encyclopedia of Electrochemical Power Sources, Secondary Batteries – Lithium Rechargeable Systems* (Elsevier Science Limited, London, 2011), pp. 27–39

110. O. Chusid, Y. Ein Ely, D. Aurbach, J. Power Sources. **43–44**, 47 (1993)
111. K. Kanamura, H. Tamura, Z. Takehara, J. Electroanal. Chem. **333**, 127 (1992)
112. K. Kanamura, H. Tamura, S. Shiraishi, Z. Takehara, J. Electrochem. Soc. **142**, 340 (1995)
113. K. Kanamura, *Electrolytes for Lithium Batteries, Fluorinated Materials for Energy Conversion Chap. 11* (Elsevier, London, 2005), pp. 253–266
114. B. Jagger, M. Pasta, Joule. **7**, 2228 (2023)
115. K. Liu, A. Pei, H.R. Lee, B. Kong, N. Liu, D. Lin, Y. Liu, C. Liu, P.-C. Hsu, Z. Bao, Y. Cui, J. Am. Chem. Soc. **139**, 4815 (2017)
116. S. Choudhury, S. Stalin, D. Vu, A. Warren, Y. Deng, P. Biswal, L.A. Archer, Nat. Commun. **10**, 4398 (2019)
117. R. Tamate, Y. Peng, Y. Kamiyama, K. Nishikawa, Adv. Mater. **35**, 2211679 (2023)
118. H. Wang, Y. Peng, R. Tamate, K. Nishikawa, S. Nakanishi, J. Power Sources. **641**, 236801 (2025)
119. K. Nishikawa, K. Shinoda, J. Phis Chem. Lett. **12**, 3922 (2022)
120. M. Nagasaki, K. Kanamura, ACS Appl. Energy Mater. **2**, 3896 (2019)
121. J. Takeyoshi, N. Kobori, K. Kanamura, Electrochemistry. **88**, 540 (2020)
122. Y. Yamada, Electrochemistry. **9**, 559 (2017)
123. S. Ko, T. Obukata, T. Shimada, N. Takenaka, M. Nakayama, A. Yamada, Y. Yamada, Nat. Energy. **7**, 1217 (2022)

**Publisher's note** Springer Nature remains neutral with regard to jurisdictional claims in published maps and institutional affiliations.